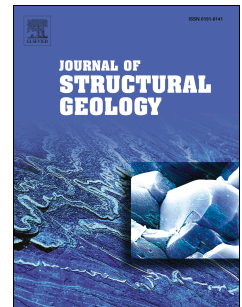


Accepted Manuscript

Jurassic extension and Cenozoic inversion tectonics in the Asturian Basin, NW Iberian Peninsula: 3D structural model and kinematic evolution

Hodei Uzkeda, Mayte Bulnes, Josep Poblet, José Carlos García-Ramos, Laura Piñuela



PII: S0191-8141(16)30105-5

DOI: [10.1016/j.jsg.2016.08.003](https://doi.org/10.1016/j.jsg.2016.08.003)

Reference: SG 3371

To appear in: *Journal of Structural Geology*

Received Date: 10 March 2016

Revised Date: 22 July 2016

Accepted Date: 7 August 2016

Please cite this article as: Uzkeda, H., Bulnes, M., Poblet, J., García-Ramos, J.C., Piñuela, L., Jurassic extension and Cenozoic inversion tectonics in the Asturian Basin, NW Iberian Peninsula: 3D structural model and kinematic evolution, *Journal of Structural Geology* (2016), doi: 10.1016/j.jsg.2016.08.003.

This is a PDF file of an unedited manuscript that has been accepted for publication. As a service to our customers we are providing this early version of the manuscript. The manuscript will undergo copyediting, typesetting, and review of the resulting proof before it is published in its final form. Please note that during the production process errors may be discovered which could affect the content, and all legal disclaimers that apply to the journal pertain.

Jurassic extension and Cenozoic inversion tectonics in the Asturian Basin, NW Iberian Peninsula: 3D structural model and kinematic evolution

Hodei Uzkeda ^{1*}, Mayte Bulnes ¹, Josep Poblet ¹, José Carlos García-Ramos ² and Laura Piñuela ²

¹ Departamento de Geología, Universidad de Oviedo, C/Jesús Arias de Velasco s/n, 33005 Oviedo, Spain. E-mail (Uzkeda): hodei@geol.uniovi.es, E-mail (Bulnes): maite@geol.uniovi.es, E-mail (Poblet): jpoblet@geol.uniovi.es

² Museo del Jurásico de Asturias (MUJA), Rasa de San Telmo s/n, 33328 Colunga, Spain. E-mail (García-Ramos): jcgramos.muja@gmail.com, E-mail (Piñuela): lpinuela.muja@gmail.com

* corresponding author

Abstract

We constructed a geological map, a 3D model and cross-sections, carried out a structural analysis, determined the stress fields and tectonic transport vectors, restored a cross section and performed a subsidence analysis to unravel the kinematic evolution of the NE emerged portion of the Asturian Basin (NW Iberian Peninsula), where Jurassic rocks crop out. The major folds run NW-SE, normal faults exhibit three dominant orientations: NW-SE, NE-SW and E-W, and thrusts display E-W strikes. After Upper Triassic-Lower Jurassic thermal subsidence, Middle Jurassic doming occurred, accompanied by normal faulting, high heat flow and basin uplift, followed by Upper Jurassic high-rate basin subsidence. Another extensional event, possibly during Late Jurassic-Early Cretaceous, caused an increment in the normal faults displacement. A contractional event, probably of Cenozoic

age, led to selective and irregularly distributed buttressing and fault reactivation as reverse or strike-slip faults, and folding and/or offset of some previous faults by new generation folds and thrusts. The Middle Jurassic event could be a precursor of the Bay of Biscay and North Atlantic opening that occurred from Late Jurassic to Early Cretaceous, whereas the Cenozoic event would be responsible for the Pyrenean and Cantabrian ranges and the partial closure of the Bay of Biscay.

Keywords

Normal fault, reverse fault, reactivated fault, inversion tectonics, basin inversion, Jurassic, Asturian Basin

1. Introduction

The Asturian Basin is a Permian-Mesozoic extensional basin, located in the NW portion of the Iberian Peninsula, partially inverted during the Cenozoic as a result of an Alpine age contractional event that caused the elevation of the Cantabrian Mountains, the formation of the Pyrenean chain to the E and the partial closure of the Bay of Biscay to the N (Figure 1). The main features of this basin have been previously described, however, there is still a lack of understanding of the relevance as well as the precise age of the extensional and contractional structures that define the current framework of the basin, especially of its eastern sector (e.g., Beroiz et al., 1972a, 1972b; Pignatelli et al., 1972; Suárez Rodríguez, 1988; Lepvrier and Martínez-García, 1990; Riaza Molina, 1996; Alonso et al., 2009; Cadenas, 2013; Martín et al., 2013; Uzkeda, 2013; Uzkeda et al., 2013).

In order to characterize the different structures and the modes of inversion, relating them to the influence exerted by old extensional faults as well as the behaviour of inherited structures, we constructed a geological map, a 3D model and several cross sections, and performed a structural analysis of the study area, that is, the NE emerged portion of the Asturian Basin where Jurassic

rocks crop out (Figure 1). In addition, we attempted to gain insight regarding the evolution of the Asturian Basin by carrying out a comprehensive analysis of the study area which includes determining the tectono-thermal regime, the stress field, the tectonic transport vectors and the amounts of extension and contraction during the different events.

Apart from the purely scientific perspective, the Jurassic rocks exposed in the study area are also interesting from the points of view of hydrogeology (Menéndez Casares et al., 2004), engineering geology (Gutiérrez Claverol et al., 2008), hydrocarbon source rocks with type II kerogen (Soler et al., 1981; Valenzuela et al., 1986; Valenzuela, 1988; Suárez-Ruiz, 1989; García-Ramos and Gutiérrez Claverol, 1995; Suárez-Ruiz and Prado, 1995; Ríaza Molina, 1996; Borrego et al., 1997; García-Ramos et al., 2006, 2008; Bádenas et al., 2013), jet jewellery (e.g., Campón et al., 1978; Suárez-Ruiz et al., 2006; García-Ramos et al., 2008), vertebrate dinosaur palaeontology (Ruiz-Omeñaca et al., 2006; Lockley et al., 2007) and heritage protection and conservation (Carcavilla et al., 2010; García-Ramos, 2013). Unravelling the structure of these rocks is also important because a hydrocarbon investigation permit has been requested by an oil company to explore the subsurface beneath the study area, which, in turn, belongs to a Spanish State reserve acreage for CO₂ storage.

2. Geological setting

The studied area is situated in the NE part of the emerged portion of the Asturian Basin (Figure 1), located in the N continental margin of Iberia. This basin has an infilling of Permian-Mesozoic materials unconformably overlying a Palaeozoic basement of Cambrian to Carboniferous age. These basement rocks are involved into a fold-and-thrust belt located in the foreland of the Variscan Orogen of W Iberia, known as Cantabrian Zone, generated mainly during the Carboniferous. The Cantabrian Zone, as well as hinterland portions of the orogen, displays an orocline geometry around an approximately E-W axis called Asturian or Ibero-Armorican Arch and the Asturian Basin sits on top of the N branch of the arch. The basement, as well as the Permian and part of the Mesozoic

deposits, have undergone diverse extensional episodes related to a Permian-Triassic continental rifting (e.g., Suárez Rodríguez, 1988; Lepvrier and Martínez-García, 1990; Riaza Molina, 1996; García-Ramos, 1997) and to the Late Jurassic-Early Cretaceous opening of the Bay of Biscay and North Atlantic (e.g. Lepvrier and Martínez-García, 1990; Riaza Molina, 1996; Aurell et al., 2002, 2003; Uzkeda et al., 2013). These rocks, in conjunction with the remaining Mesozoic and Cenozoic deposits, were deformed during the Alpine contraction resulting from the convergence of the Iberian and Eurasian plates that, in this region, took place during the Cenozoic (Alonso et al., 1996; Riaza Molina, 1996). It caused uplift and partial inversion of the Asturian Basin through reactivation of previous structures (e.g., Julivert et al., 1971; Lepvrier and Martínez-García, 1990; Alonso et al., 1996; Riaza Molina, 1996; Pulgar et al., 1999; Uzkeda et al., 2013). The evolution of the area continued with the episodic uplift of marine abrasion platforms (Flor, 1983; Mary, 1983; Álvarez-Marrón et al, 2008 amongst others) and neotectonic activity such as occasional outcrop-scale faulting (Gutiérrez Claverol et al., 2006) and small magnitude earthquakes (López-Fernández et al., 2004).

3. Stratigraphy

Five Jurassic lithostratigraphic units were identified in the study area, one of them divided into two members. From older to younger they are (Figure 2):

- 1) The Gijón Fm. has a Rhaetian (Upper Triassic) to Lower Sinemurian age (Suárez Vega, 1974; Barrón et al., 2002, 2006). It is a 250 m thick predominantly carbonate unit (grey limestones, magnesian limestones and dolostones) with several levels of claystones and marls, evaporites and dissolution carbonate breccias. The recorded facies associations can be interpreted as deposited in a sabkha to hypersaline coastal lagoon environment in a tidal flat system, gradually evolving to a bioclastic and oolitic bar-lagoon complex (Valenzuela et al., 1986; Aurell et al., 2002; González et al., 2004; García-Ramos et al., 2006).

2) The Rodiles Fm., which is assigned to the Upper Sinemurian to Lower Bajocian (Suárez Vega, 1974), is divided into the Buerres and the overlying Santa Mera members (Valenzuela et al., 1986). The Buerres Mb. has an Upper Sinemurian age (Suárez Vega, 1974; Comas Rengifo and Goy, 2010; Goy et al., 2010), consists of alternations of grey nodular limestones and less abundant marls, and its thickness is around 61 m. The age of the Santa Mera Mb. ranges from Pliensbachian to Lower Bajocian, although the age of its top varies from Lower Pliensbachian to Lower Bajocian (Suárez Vega, 1974; Fernández-López and Suárez-Vega, 1981). It is an alternation of grey marls and limestones with similar abundances of both lithologies (Bádenas et al., 2012), including important levels of black shales of Pliensbachian and Lower Toarcian age (García-Ramos et al., 1992, 2011; Suarez-Ruiz and Prado, 1995; Bádenas et al., 2013). The thickness of Santa Mera Mb. ranges from 50 m to over 152 m. The Rodiles succession was deposited on a carbonate ramp at diverse depths, from above fair weather wave base to below storm wave base. The black shale episodes accumulated in local intrashelf depocentres possibly generated by differential subsidence due to vertical movements.

3) The Vega Fm. has been attributed to the Kimmeridgian (Schudack and Schudack, 2002). It is a 130 m thick unit composed of alternating white, grey and reddish sandstones, with red mudstones and some conglomeratic beds, ordered in minor fining-upward cycles. They represent fluvial deposits formed by ephemeral and highly sinuous streams separated by inter-channel areas with calcareous paleosols (calcretes) (Gutierrez and Sheldon, 2012) and sporadic ponds with high microbial activity which gave rise to grey limestones with oncoids. These ponds were partly fed by a number of freshwater carbonate-rich springs coming from faulted zones that affected the limestones and dolomites of the underlying Jurassic units (García-Ramos et al., 2010a, Arenas et al., 2015; Delvene et al., 2016; Lozano et al., 2016). This unit lies unconformably over the Rodiles Fm.

4) The Tereñes Fm. was deposited during the Late Kimmeridgian (Schudack and Schudack, 2002). This unit is formed by dark grey marls with interbedded shell beds of brackish invertebrate fauna

(bivalves, gastropods and ostracods) and, more sporadic, grey sandstones and limestones. Several beds with high concentrations of organic matter are common in its lower part forming black shales. The sedimentary environment responsible for this unit is a shelf lagoon separated from the open ocean by a threshold or barrier of tectonic origin that impeded the entry of stenohaline fauna (García-Ramos et al., 2010b; Fürsich et al., 2012). Its thickness oscillates between 60 and 160 m, possibly because of transition to the Vega and Lastres formations and fault activity simultaneous with its deposition.

5) The Lastres Fm., Kimmeridgian in age (Dubar and Mousterde, 1957; Olóriz et al., 1988; Schudack and Schudack, 2002), is composed of sandstones, mudstones and marls with occasional conglomeratic lenses. The depositional environment consists of coastal wetlands including fluvial-dominated deltas prograding on a shelf lagoon. The short-term transgressive events are recorded by laterally extensive shell beds with abundant bivalves and gastropods (Valenzuela et al., 1986; García-Ramos et al., 2006). The minimum thickness of this formation is about 350 m.

4. Map-scale structure

Detailed geological mapping and structural data collection (Figure 3) were carried out. Both were the foundation for the construction of a 3D structural model (Figure 4) created using the dip-domains method in 3D (Fernández et al., 2004). Both the geological map and the 3D model were employed to generate several geological cross-sections. In addition, we performed a geological photointerpretation of detailed aerial photographs of the tidal portion of the coast, shot from a small plane, to improve the geological map and study the orientation of the fractures (faults and joints).

Since bedding usually dips from 10° to 25° to the NE in the study area, rocks become progressively older landwards, i.e. to the SW (Figure 3). However, close to some faults beds there are sub-vertical dips.

Most map-scale faults included in the 3D geological model exhibit normal displacements (Figure 4). The normal faults strike typically NW-SE, NE-SW and E-W to ESE-WNW (Figures 3 and 5a). The two largest faults mapped, located in the E of the study area, strike NW-SE and are illustrated in cross-sections A-A' and B-B' (Figure 6). The one located to the NE also appears in cross-section C-C', whereas the other does not as it bends to an E-W direction just to the S of cross section line B-B' (Figure 3). The southwestern fault dips about 60°-70° to the NE, whereas the northeastern fault dips about 50° to the SW, although its dip decreases in cross section C-C'. The northeastern fault, which exhibits more displacement than the southwestern fault, is interpreted as the main one with the other one as a related antithetic fault. The maximum fault displacement (around 250 m) occurs in section B-B' decreasing along strike. Normal faults with NE-SW strikes are especially abundant in the western sector of the study area. The best map-scale examples are two faults that crop out along La Conejera Inlet and dip in opposite senses (Figure 3 and section 1-1' in figure 7). The northwestern fault dips about 55°-75° to the SE and displays a fault separation of 60-65 m, whereas the southeastern fault dips from 45° to 80° to the NW and has a fault separation of 45 m. The two most significant E-W to ESE-WNW faults at map-scale are located at El Sable and Lastres beaches, to the N and to the E of the study area respectively (Figure 3, sections A-A' and B-B' in figure 6, and sections 2-2' and 4-4' in figure 7). The northern one dips around 70° to the N and exhibits a normal fault displacement of about 45 m, and the eastern one dips around 50° to the N and its estimated displacement is about 100 m.

Reverse faults are much less abundant than normal faults and run mainly E-W (Figure 5b). Cartographic-scale, reverse faults can be found in the eastern portion of the study area at the Lastres Beach and to the E of La Griega Beach (Figure 3). These faults dip from moderately to steeply to the N and exhibit displacements around 10-15 m (sections B-B' and C-C' in figure 6).

Concerning the folds, they have orientations similar to those of the faults. Except for the smooth folds parallel to the NE-SW faults that crop out at La Conejera Inlet located to western part of the studied area, and the WNW-ENE syncline that crops out at the Lastres and La Griega beaches to the

174 E of the study area, cartographic-scale folds display NW-SE axial traces (Figure 3). One of the most
 175 significant NW-SE folds runs from the Lastres Beach to El Sable Beach. In the hangingwall of a
 176 large NW-SE normal fault described above, bed dips increase as approaching the fault, reaching
 177 values close to 40° and depicting a rollover anticline geometry (sections A-A' and B-B' in figure 6,
 178 and section 4-4' in figure 7). The fold is a gentle (interlimb angle about 150°), rounded and
 179 relatively asymmetric structure with a steeper northeastern limb. Other NW-SE, map-scale folds
 180 have been mapped in the central sector of the study area (Figure 3). They are gentle (interlimb
 181 angles over 160°), upright structures with rounded geometry and low half-wavelength/amplitude
 182 ratio (section 3-3' in figure 7).

183

184 **5. Minor scale structures**

185 *5.1. Faults*

186 *5.1.1. Normal faults*

187 Most faults in the studied area are normal faults. They show four preferred orientations: NE-SW,
 188 NW-SE, E-W and NNW-SSE (Figure 8a), similar to the larger scale ones (Figure 3). The kinematic
 189 indicators identified on the fault surfaces (striae) of all the different sets indicate an approximately
 190 dip-slip movement. The NE-SW set is frequent in the western part of the study area, being relatively
 191 scarce in the rest. Their strikes range from N040E to N070E and they dip from 45° to 90° to both the
 192 NW (more common) and the SE. The NW-SE faults are the most numerous in the eastern portion of
 193 the study area. They strike from N030W to N060W and dip between 35° to almost vertical to the
 194 NE (more frequently) and to the SW. Much less common are the E-W faults, which may dip
 195 between 45° and 90° either to the S or, more commonly, to the N. The least abundant normal faults
 196 are the NNW-SSE ones, which are mainly restricted to the southeastern portion of the studied
 197 region. They strike around N010W and dip from 40° to 80° to the E and to the W.

198 5.1.2. Reverse faults

199 The reverse faults have a dominant E-W strike, ranging from N060E to N110E, with a maximum
 200 between N070E and N080E (Figure 8b). Their dips, both to the N (more common) and to the S,
 201 have a wide range, from 5° to about 80°. Their kinematic indicators (striae) point out a dip-slip
 202 movement, although a small strike-slip component has been identified on some fault surfaces. There
 203 are other reverse faults with strikes such as NE-SW, NW-SE and even N-S, much less frequent than
 204 the E-W faults (Figure 8b). The NE-SW faults, whose strikes vary from N020E to N060E, dip both
 205 to the NW and to the SE (more commonly) between 10° and almost 70°. The only recorded striae
 206 indicate a dip-slip movement with a slight right-lateral strike-slip component. Two NW-SE reverse
 207 faults dipping to the SW (30° and 80°) have been measured. Only one N-S reverse fault, whose dip
 208 is 75° to the E, has been recognized in the field.

209 5.1.3. Right-lateral faults

210 These dextral faults commonly strike NW-SE, dipping around 50° to both the NE and the SW
 211 (Figure 8c). It is possible that these right-lateral faults correspond to reactivated normal faults since
 212 faults with this orientation showing two superposed movements are described below. There are also
 213 WNW-ESE faults to the W of the study area, whereas in the eastern region faults have NNW-SSE
 214 strikes. The WNW-ESE faults strike from N040W to N090W and dip to both the N and the S with
 215 values over 55°. Their striae indicate almost pure strike-slip movements. The NNW-SSE faults are
 216 less frequent, exhibit strikes ranging from N000E to N040W and dip mainly to the W between 40°
 217 to almost vertical, being more common the higher values. Their surfaces contain strike-slip striae
 218 with a minor dip-slip, commonly reverse, component.

219 5.1.4. Left-lateral faults

220 The most common left-lateral faults strike NE-SW, although faults with NNE-SSW orientation
 221 occur as well (Figure 8d). This strike coincides with one of the orientations for the normal faults. It
 222 is therefore possible that some of them resulted from reactivation of older normal faults. The NE-

SW faults strike around N060E and dip to both the SE and the NW, with values that vary from 40° to 70°. Their striae indicate a strike-slip movement which can have a small reverse dip-slip component. The NNE-SSW faults have strikes ranging from N010E to N020E and dips over 60° to the W or E.

5.2. Reactivated faults

5.2.1. Normal and right-lateral faults

These faults show two sets of striae pointing to an old normal dip-slip movement and a later approximately pure strike-slip one (Figure 8e). Two fault sets have been identified: WNW-ESE and NNW-SSE. The WNW-ESE fault set is the most frequent and their dips range from 40° to 60° to the SSW. The NNW-SSE fault set is restricted to the eastern portion of the study area and dip around 50°-65° to the WSW. Despite the lack of superposed kinematic indicators associated with the cartographic-scale normal faults with these strikes (Figure 3), they might have been also reactivated as right-lateral faults.

5.2.2. Normal and left-lateral faults

Their predominant strike is NE-SW (Figure 8f), coincident with that of some major normal faults which might have also undergone an approximately pure strike-slip reactivation. These faults dip between 35° and over 60° to the SE. Two other normal faults reactivated as left-lateral faults with different orientation were found, a N-S fault that dips around 50° to the E, and an E-W fault that dips 80° to the S.

5.2.3. Normal and reverse faults

Only two faults display kinematic indicators pointing to a normal displacement and a sub-parallel, approximately dip-slip reverse displacement. The first one is a WNW-ESE striking fault that dips steeply to the NNE, and the second one has a WSW-ENE strike and dips to the NNW (Figure 8g).

246 5.3. Folds

247 More than 30 folds were analysed with sizes in the metric to decametric range (Figure 9). They are
 248 located preferentially in the hangingwalls of steep dipping faults. The fold axes and axial surfaces
 249 are sub-parallel to the strike of the faults, and in general, the fold axes are sub-horizontal and the
 250 axial planes sub-vertical. This spatial relationship between folds and faults might be regarded as a
 251 buttressing effect in some cases, so that the orientation of the folds would be controlled not only by
 252 the main stresses direction but also by the trend of the faults nearby. The folds measured have two
 253 preferred orientations: E-W and NE-SW.

254 The E-W folds are the most abundant and exhibit fold axes ranging between WNW-ESE to WSW-
 255 ENE (stations 2, 3, 5, 6, 8 to 19 in figure 9 and figures 10a, 10b, 10c, 10d and 10f). In general, they
 256 are open to gentle folds with moderately dipping limbs, steeply inclined to sub-vertical axial planes
 257 and gently plunging to sub-horizontal fold axes. They are usually parallel, rounded and relatively
 258 symmetric folds, although examples of highly asymmetric folds occur as well (Figure 10c). One of
 259 the most representative examples of relationships between folds and E-W faults can be found at La
 260 Griega Beach in the southeastern part of the study area (stations 8 and 10 in figure 9). At locality 8
 261 a metre-scale anticline (Figure 10d) with two second-order folds (one syncline and one anticline) in
 262 its southern limb crop out (geological map and section A-A' in figure 10f). All these folds are
 263 bounded by two sub-vertical E-W faults to the N and to the S. These folds are open and have
 264 steeply dipping to upright axial planes and gently plunging to sub-horizontal fold axes. The plunge
 265 of the metre-scale anticline is responsible for the scissor movement along the southern bounding
 266 fault (compare section A-A' and B-B' in figure 10f). We interpret that these folds resulted from a
 267 buttressing effect within the two sub-vertical faults.

268 The best examples of NE-SW folds are located in the sunken block of a steeply dipping reverse NE-
 269 SW fault to the W of La Griega Beach (station 7 in figure 9). The two anticlines are gentle folds
 270 slightly tighter than the open syncline in between them, especially the one close to the fault (Figure

10e). They exhibit steeply dipping (anticlines) to sub-vertical (syncline) axial planes and sub-horizontal fold axes, except for one of the anticlines which plunges gently. All the folds are relatively rounded, parallel and symmetric structures; the northern limb of the southernmost anticline is sub-parallel to the fault.

5.4. Joints

In general, joints form orthogonal systems composed of two families (Figure 11) whose orientation varies depending on the region. To the E of the study area the two sets strike approximately N-S and E-W, whereas to the W they strike NW-SE and NE-SW. Joints are best developed in the limestones of the Rodiles Fm. and in the sandstones of the Vega Fm. The N-S joints strike between N030W and N020E, and dip from 65° to 90° both to the W (more commonly) and to the E. The E-W joints appear typically accompanying the previous ones (Figure 8h). Their strikes range from N070E to N120E and they dip over 70° to the N or to the S. The NW-SE joints strike ranges between N040W and N070W, and they dip steeply (over 70°) mainly to the NE. The strike of the NE-SW joints, developed in the same outcrops as the previous ones, ranges from N030E to N060E and their dip between 70° and 85° both to the NW (more common) and to the SE.

6. Tectonics-sedimentation relationships and age of structures

The age of some faults has been deduced from: a) variation in the age of the top of the Rodiles Fm., b) thickness changes of the Rodiles and Tereñes formations, and c) occurrence of hot spring-related microbialites and associated breccias within the Vega Fm.

6.1. NE-SW faults

The age of the NE-SW normal faults located in La Conejera Inlet (Figure 3 and section 1-1' in figure 7) has been estimated by comparison of two stratigraphic columns constructed by Suárez Vega (1974). In the uplifted fault block (footwall) the Rodiles Fm. top has an Upper Toarcian age

(Lower Jurassic), whereas in the sunken fault block (hangingwall) it reaches a Lower Bajocian age (Middle Jurassic) (section A-A' in Figure 12). Additionally the hangingwall series is 30 m thicker than the footwall succession. This supports a possible normal fault activity during this period; the fault could have started to be active at some point between the Upper Toarcian and the Kimmeridgian (Late Jurassic), i.e., before the sedimentation of the unconformably overlying Vega Fm. (Uzkeda et al., 2013). In particular, it could have started in Aalenian times (Middle Jurassic), when rapid lateral facies and thickness changes, suggesting important fault reactivation, became common throughout the Asturian Basin (Fernández-López and Suárez Vega, 1974; Valenzuela et al., 1989). Considering the amount of present-day, normal displacement along this NE-SW fault, it must have also been active after the unconformity between the Rodiles and Vega Fm. Summarizing, this NE-SW fault would have been active during sedimentation of the upper part of the Rodiles Fm. before sedimentation of the Vega Fm. (from Late Early Jurassic to Late Jurassic) and again during or after sedimentation of the Vega Fm.

6.2. NW-SE faults

Two stratigraphic columns drawn by Suárez Vega (1974) around the Lastres and La Griega beaches, separated by a large NW-SE normal fault (Figures 3 and 6), show that the age of the Rodiles Fm. top in the uplifted fault block (footwall) is Middle Toarcian (Lower Jurassic), whereas it reaches the Lower Bajocian (Middle Jurassic) in the sunken fault block (hangingwall), where this stratigraphic unit is 30 m thicker (section B-B' in Figure 12). Thus, the fault might have been synchronous with the sedimentation of the upper part of Rodiles Fm. (Middle Toarcian to Lower Bajocian) or posterior to its sedimentation and previous to that of the unconformably overlying Vega Fm. Therefore, this fault would have acted approximately at the same time as the NE-SW fault described above. The Tereñes Fm., of Kimmeridgian (Late Jurassic) age, also exhibits thickness variations on both fault blocks (sections A-A' and B-B' in figure 6); its thickness is about 60-70 m in the footwall, whereas it is greater than 100 m in the hangingwall. In spite of the particular facies of the Tereñes Fm., this thickness change can be attributed to the activity of this

normal fault contemporaneous to the Tereñes Fm. deposition. This major fault also offsets the Lastres Fm.; thus, the fault would have also been active during or after the sedimentation of the Lastres Fm. We can conclude that this NW-SE fault would have been active continuously or intermittently during sedimentation of the upper part of the Rodiles Fm. and during sedimentation of the Tereñes Fm. (from Late Early Jurassic to Late Jurassic), and during or after sedimentation of the Lastres Fm.

6.3. E-W faults

Some E-W faults located in the Lastres and La Griega beaches (Figure 3) display evidence of having been active during deposition of the Vega Fm. According to García-Ramos et al. (2010a), Arenas et al. (2015) and Lozano et al. (2016) the carbonate deposits with abundant oncoids and associated breccias that crop out in this area within the Vega Fm. are related to fault activity for the following reasons: a) they consist of lacustrine and palustrine facies located close to the faults that are not typical of the arid environment responsible for the Vega Fm., requiring a carbonate-rich spring, fed by the underlying carbonate units; b) the breccias associated with the oncoids could be attributed to fault activity; and c) the orientation of the relatively high-gradient gullies associated with these spring-fed water currents is different from the main axial siliciclastic fluvial system in the region, pointing to a certain topographic control by the fault. Summarizing, these E-W faults would have been active during deposition of part of the Vega Fm. of Kimmeridgian age (Late Jurassic).

6.4. Structural chronology

In addition to the absolute ages of the main faults presented above, we have attempted to establish a relative timing for other structures developed in the study area.

As the strike of some joints varies along the limbs and hinge of the folds but keep an approximately constant angular relationship with bedding (Figure 13a), we suggest that some joints might be older than some folds. Nevertheless, it could be that bedding acted as a mechanical anisotropy which

deflected the joint forming stresses, and therefore, joints would be younger than folds. No conclusive temporal relationships between joints and faults have been established.

Unfortunately, we have not been able to identify field cross-cutting relationships between the different sets of normal faults. However, there is evidence of: a) normal faults reactivated as reverse and strike-slip faults (Figures 8e, 8f and 8g), b) normal faults cut and offset by thrusts (Figures 13b and 13c; Figure 11 in Alonso et al., 2009), and c) contractional folds and thrusts resulting from buttressing against older normal faults (Figure 10f; Figures 19a and 20 in Uzkeda et al., 2013). These three observations point to normal faults pre-dating the reverse and strike-slip ones. The temporal relationship between reverse and strike-slip faults is unclear.

The temporal relationship between folds and faults is complex. Some folds have been interpreted as rollover folds contemporaneous with normal faults (sections A-A' and B-B' in figure 6, and section 1-1' in figure 7). However, it is also common to find normal faults offset along bedding planes as a consequence of flexural-slip occurred during folding and sets of originally parallel normal faults varying their dip depending on the structural position they occupy within a fold (Figure 13b) indicating that some folds, probably of contractional origin, postdate normal faults. We believe that contractional folds and reverse faults/thrusts are simultaneous in a broad sense because we have observed the following relationships: a) contractional folds developed after reverse faults/thrusts (figure 13b illustrates thrusts varying their dips as passing from one fold limb to the fold hinge and to the other fold limb); b) contractional folds coeval to reverse faults/thrusts (section B-B' in figure 6 illustrates a fault-propagation fold related to a thrust verging to the SW); and c) contractional folds initiated before reverse faults/thrusts (in figure 13c a thrust offsetting both limbs of a syncline is displayed, so that the thrust is slightly folded by the syncline but much less folded than the rocks involved in the fold).

To conclude, the temporal sequence of development of the structures from older to younger would broadly be: 1) extensional structures including various sets of normal faults and related folds

(rollovers), the NW-SE faults being the oldest set to initiate and the E-W faults the youngest set to develop; and 2) contractional structures including folds (some of them related to thrusts) developed slightly before, during and after the development of reverse faults and thrusts. The main effects of the contractional event on some of the previous extensional structures consisted of reactivation of extensional faults, extensional faults deformed by folds and offset by thrusts and buttressing effects. The strike-slip faults may have been active in a late period during the contractional event.

7. Stress analysis

We performed a stress analysis using the kinematic indicators collected on fault surfaces. Given that the area has undergone at least two different tectonic events, it is necessary to separate the data. The first group contains normal faults whose striae show approximately pure normal dip-slip movement, together with reactivated faults including two superposed generations of striae whose older motion corresponds to a normal slip. The second group is formed by faults whose kinematic indicators denote a reverse dip-slip or strike-slip movement, since we assumed that both movements took place during the same tectonic event, together with reactivated faults whose younger striae indicates reverse or strike-slip motion. We used the software FaultKin v. 5.2.4, developed by Richard W. Allmendinger, which is based on the kinematic method of Marrett and Allmendinger (1990). This software is appropriate for the study area because it is suited to regional studies in which the principal axes orientation is more important than their magnitudes. This software assumes that the principal incremental shortening and extension axes for a particular fault lay in the “movement plane” containing the slip vector and the normal vector to the fault plane, and at 45° to each of the vectors. The contouring of the shortening and extension axes of a fault array is carried out using the procedure of Kamb (1959). The directional maxima of the shortening and extension axes of the fault array is estimated using Bingham distribution statistics for axial data.

395 7.1. Stress field during the extensional event

396 All the available extensional kinematic indicators have been plotted in Figure 14a. The main
 397 extensional axis would be almost N-S and sub-horizontal (007/07). Most of the fault P and T axes
 398 are within the correct field, thus, the principal axes calculated would explain reasonably well the
 399 different sets of normal faults mapped in the studied area. However, we also performed a stress
 400 analysis separating the kinematic indicators coming from three different regions to check whether
 401 we obtained a uniform field stress or local variations occur. To the W of the study area (Figure 14b)
 402 normal faults tend to be NE-SW and include NW-SE striae. The principal extensional axis obtained
 403 would plunge gently to the NNW (342/15). In the central area (Figure 14c) normal faults strike
 404 ESE-WNW to E-W and include NNE-SSW striae. The principal extensional axis obtained is almost
 405 N-S and sub-horizontal (195/09). To the E of the study area (Figure 14d) most of the faults strike,
 406 approximately, NW-SE and have NE-SW striae. The result is a principal extensional axis gently
 407 plunging to the NE (048/07). According to these results, we conclude that local deviations occur
 408 although the principal average extensional axis has a general N-S component. Several hypotheses,
 409 and combinations of them, can be proposed to account for this feature: a) the orientation of the
 410 stress field responsible for all the normal faults was approximately constant, but the orientation of
 411 the faults in each region was conditioned by local heterogeneities such as an inherited structural
 412 framework (Lepvrier and Martínez-García, 1990). b) The orientation of the stress field responsible
 413 for the normal faults was not constant but ranging from NNW-SSE to NE-SW. c) The present-day
 414 fault distribution was caused by large-scale folding along a sub-vertical axis located to the S of the
 415 study area that occurred before the contractional event, since the orientation of the compressional
 416 stress field is approximately constant all along the study area as shown below. Unfortunately, we
 417 have no data to support or discard these three options since: a) no pre-Jurassic rocks crop out in the
 418 study area to check the influence of inherited structures; b) no data are available to prove that a
 419 stress field with different orientations through time and/or space occurred; and c) no paleomagnetic
 420 data are available to check the occurrence of rotations about vertical axes.

7.2. Stress field during the contractional event

Using all the available contractional kinematic indicators as input data we obtained a sub-horizontal N-S principal compressive axis (351/08) (Figure 14e). The presence of a moderately dipping intermediate principal axis would indicate a contractional setting with a marginal strike-slip component. We also performed a stress analysis for two separated regions. To the W of the study area the method provided a sub-horizontal N-S principal compressive axis (352/05) (Figure 14f). More to the E the analysis resulted in a sub-horizontal NNW-SSE principal compressive axis (344/05) similar to the previously obtained (Figure 14g). Thus, no variation of the principal compressive axis occurs within the study area.

8. Restoration of a geological cross-section

8.1. Choice of the geological cross-section

A geological cross-section to be properly restored must contain the tectonic transport direction. Therefore in a region where the structural framework resulted from more than one tectonic event it is necessary to identify the tectonic transport vectors for each of the events. Thus, we analysed the fault kinematic indicators for the extensional event and those for the contractional event in the study area (Figure 15). Additionally, the folds were analysed separately, as it is not always possible to determine during which event they were formed. The general orientation of the tectonic transport directions deduced using fault kinematic indicators on normal fault surfaces is N-S, although it exhibits a local deviation towards the E of the study area. The kinematic indicators of reverse faults provide a range for the tectonic transport vector around a N-S direction. The strike-slip faults, many of which correspond to reactivated normal faults, yield wider ranges but most of them are consistent with the N-S direction. The minor fold axes, assumed to be perpendicular to the tectonic transport direction, indicate broadly a N-S tectonic transport direction with slight variations, from NNW-SSE to NNE-SSW (Figure 9). The axes of major (map-scale) folds point to a NE-SW tectonic transport

direction in the central portion of the study area that passes to NNW-SSE to the E and to the W of the study area (Figure 15).

The differences between the tectonic transport directions deduced for the extensional and contractional events are relatively small and range from NNE-SSW to NE-SW with an average direction around N020E-N030E. Thus, we constructed a geological section across the eastern part of the study area following this direction which, in addition, it is sub-perpendicular to the main faults and folds in this region (Figure 16a). This cross section has been included in a regional section across the Asturian Basin constructed using data from previous sections (e.g. Beroiz et al., 1972a; Suárez Rodríguez, 1988; Alonso et al., 1996; Pulgar et al. 1999) (Figure 16b). The regional-scale section shows that the Mesozoic sequence has a regional dip of 7° to the NNE in the study area and surrounding regions. Thus, the section across the study area has been rotated 7° following a counter clockwise sense looking WNW before its restoration (Figure 16a).

8.2. *Extension and shortening estimations*

The restoration to the pre-contractional post-extensional stage, carried out using the flexural slip algorithm, is founded on the following assumptions: 1) no variation in the main fault geometry during contraction took place, although fault tilting is allowed; 2) plane-strain deformation is assumed although it may not be completely true since a certain strike-slip component during the contractional event may have taken place in the case of faults oblique to the contractional tectonic transport direction; 3) the geometry of the hangingwall of the main fault during the extensional event was a rollover anticline.

The restoration to the pre-inversion/post-extensional stage yielded a minimum shortening value of 122 m (3% shortening). Comparing this restored stage with the total restoration an extension magnitude of 500 m can be estimated (13% extension).

9. Subsidence analysis

We followed the strategy described in Allen and Allen (2013) amongst others to decipher the subsidence history of the study area through the method of backstripping. The ages of the stratigraphic units were taken from Dubar and Mousterde (1957), Suárez Vega (1974), Fernández-López and Suárez-Vega (1981), Olóriz et al. (1988), Barrón et al. (2002, 2006), Schudack and Schudack (2002), Comas Rengifo and Goy (2010), and Goy et al. (2010). The thicknesses were measured in the field, on the geological map and along sections, except for the Gijón and Lastres formations that were taken from the estimations made by Suárez Vega (1974), Valenzuela et al. (1986) and González et al. (2004). The c coefficients, that determine how porosity diminishes with burial depth, densities and surface porosities were estimated using the Sclater and Christie (1980) and Schmoker and Halley (1982) values for different lithologies taking into account the percentages of different lithologies established using the stratigraphic sections of Suárez Vega (1974) and Valenzuela et al. (1986) for each Jurassic stratigraphic unit. The minimum and maximum water depths during sedimentation were estimated based on the sedimentary environments assigned to each stratigraphic unit by Valenzuela et al. (1986) and García-Ramos and Gutiérrez Claverol (1995).

Two functions were obtained (Figure 17), one corresponding to the “total” subsidence (after removing the compaction effect) and another one corresponding to the “tectonic” subsidence (which takes into account bathymetric variations and assumes Airy isostasy). The “total” subsidence curve (Figure 17a) can be divided into four portions: an old one of approximately 10 My during the uppermost Triassic and lowermost Early Jurassic (Gijón Fm.) in which the subsidence rate is relatively fast, an intermediate period of around 30 My until Middle Jurassic (Buerres and Santa Mera members) in which subsidence is slower, an approximately 10 My period from Middle Jurassic to the lowermost Late Jurassic (hiatus separating the Rodiles and Vega formations) with no subsidence at all, and a young period of less than 10 My during Late Jurassic (Vega, Tereñes and Lastres formations) in which subsidence continues with a relatively fast rate and becomes even

faster towards younger ages. The “tectonic” subsidence curve (Figure 17b) reflects a regular and moderate subsidence for around 40 My from the uppermost Triassic to Middle Jurassic (sedimentation of the marine Gijón and Rodiles formations), a rapid uplift of approximately 10 My duration from the Middle Jurassic to the lowermost Late Jurassic (occurrence of a hiatus), and a renewed subsidence period for approximately 10 My during Late Jurassic (sedimentation of the continental Vega Fm.) with a pace comparable to that previous to the basin uplift and a tendency to become faster during the deposition of the Tereñes and Lastres formations returning to marine conditions.

10. Structural evolution

The basement of the study area belongs to the Cantabrian Zone, i.e. the outermost zone of the Iberian Variscan Massif (Lotze, 1945; Julivert et al., 1972). The main Variscan structures are thrusts and related folds developed during the Carboniferous and they have an approximately NE-SW trend in the study area (Figures 1 and 18a) as they belong to the northern branch of the Asturian or Ibero-Armorican Arc. These structures are visible in the Palaeozoic outcrops a few kilometres to the SE of the studied region (Beroiz et al., 1972a, 1972b).

The Asturian Basin initiated its development during Permian and Triassic times. At this time a continental rift defined the main structural directions of the basin: NW-SE, NE-SW and E-W (Suárez Rodríguez, 1988; Lepvrier and Martínez-García, 1990) (Figure 18b). Given the coincidence between the orientation of some Permian-Triassic faults and that of previous Late Palaeozoic structures it is possible that not all the faults were of new generation but some of them (especially the NE-SW oriented) might come from the reactivation of older ones. After a period of relative tectonic quiescence during most of the Early Jurassic, interpreted as thermal subsidence related to the Permian-Triassic continental rifting event, an extensional period took place from the oldest Early Jurassic to the middle Late Jurassic. During this event the NW-SE faults were the first set to

be active (Figure 18c), then the NE-SW ones (Figure 18d) and, finally, the E-W faults (Figure 18e), including some overlap in time (Figure 17b). Fault-related folds, such as rollovers, would have been created by the activity of these faults. Some of the NW-SE faults might correspond to the reactivation of Permian-Triassic normal structures, whereas some of the NE-SW faults could be reactivated Variscan thrusts. The activity of these faults during this extensional event, compatible with a N-S main extensional axis, was accompanied by a rapid basin uplift causing its emersion, a hiatus and an unconformity, and by high thermal flow (Figure 17b). The fault activity started before the hiatus and extended after it. Although the global sea level rose during this period (e.g., Haq et al., 1987; Hallam, 1988), the basin uplift suffered was enough to pass from marine conditions (Rodiles Fm.) to a continental environment (Vega Fm.). The heat flow caused the maturity of the organic matter present in the sediments (Suárez-Ruiz, 1989), the generation of microbialites within the Vega Fm. related to hydrothermal springs (e.g., Lozano et al., 2016) and is consistent with the 185 ± 28 Ma age (Late Triassic–lowermost Late Jurassic) attributed to the hydrothermal fluids responsible for fluorite mineralizations documented in the Asturian Basin to the E and W of the study area (Sánchez et al., 2006; 2010). This uppermost Early Jurassic-middle Late Jurassic tectono-thermal extensional event could be interpreted as an embryonic stage of the later Bay of Biscay and North Atlantic opening. The approximately simultaneous activity of faults with different orientations, coupled with basin emersion due to uplift and high thermal flow, could be explained assuming large-scale doming (Pujalte et al., 2014). Basin subsidence resumed at a fast rate during the Late Jurassic possibly related to the proper Bay of Biscay and North Atlantic opening from Late Jurassic to Early Cretaceous (Pujalte et al., 2004). This event was recorded in the study area as an increment in the normal displacements along some NE-SW and NW-SE faults since the Middle Jurassic displacements estimated for them are smaller than their current normal displacements. The succession of extensional events proposed for the study area is similar to that documented in adjacent regions such as the Basque-Cantabrian Basin (e.g., Robles et al., 2004), Iberian Basin

where they are slightly older (e.g., Salas and Casas, 1993), and Bristol Channel Basin (e.g., Van Hoorn, 1987; Ziegler, 1989).

During the Cenozoic, the Alpine contraction resulting from the convergence between the Iberian and Eurasian plates was responsible for the generation of the Pyrenean Range to the E of the study area (e.g., Boillot and Capdevila, 1977), the partial closure of the Bay of Biscay to the N (e.g., Le Pichon and Sibuet, 1971), the uplift of the Cantabrian Mountains to the S (e.g., Alonso et al., 1996) and the partial inversion of the Asturian Basin (Figure 18f). In the study area this contractional event caused reactivation of some normal faults, whereas others were offset by contractional faults, deformed by contractional folds and/or responsible for a buttressing effect. Depending on the angle between the N-S shortening and the inherited normal faults, they were more prone to be reactivated as either reverse (normal faults approximately perpendicular to the N-S compressional vector) or strike-slip faults (where they formed a more acute angle). The type of fault reactivation was also influenced by the fault dip; faults oblique to the N-S shortening vector acted as reverse if they had gentle dips and as strike-slip when they had steeper dips. The older NW-SE normal faults tended to be reactivated as right-lateral faults, whereas the NE-SW were more likely to move as left-lateral. The competence contrast between the rocks in both blocks of the inherited faults had also influence in the response to the contractional event. Thus, faults separating relatively incompetent materials in the hangingwall from more competent rocks in the footwall operated, commonly, as buttresses instead of being reactivated. Buttressing is also favoured where previous faults exhibit E-W strikes, although different orientations such as NE-SW are possible too, and steep dips above 50°-60°. The N-S shortening caused new folds, some of them related to contractional faults and some unrelated, and some of them due to buttressing. Additionally, a certain amount of tightening of the pre-existing, extensional rollover folds occurred.

570 11. Conclusions

571 The Jurassic rocks of the studied area, located to the NE of the emerged part of the Asturian Basin,
 572 are affected by small-scale faults (normal, reverse, thrust and strike slip) and folds, though, normal
 573 faults predominate. The largest structures are two NW-SE normal faults and an associated rollover,
 574 and NW-SE open folds. Deformation is small so that bedding dips gently to the N, except for some
 575 areas close to some faults, where folds crop out approximately parallel to the strike of the faults.

576 The temporal relationships between the structures indicate that normal faults and related folds
 577 predate a second generation of structures including thrusts, folds and reactivation of old structures.

578 From the Late Triassic to the lower part of the Middle Jurassic basin tectonic subsidence,
 579 interpreted as thermal subsidence related to a Permian-Triassic rifting event, took place in the study
 580 area. From the uppermost Early Jurassic to the middle Late Jurassic a N-S, with local variations
 581 ranging from NE-SW to NW-SE, extensional tectono-thermal event occurred. It caused NW-SE,
 582 NE-SW and E-W normal faults, some of them including rollover folds, which could result from the
 583 reactivation of older Variscan or Permian-Triassic features, high thermal flow, and tectonic uplift of
 584 the marine basin with its consequent emersion and generation of a stratigraphic hiatus. This tectono-
 585 thermal event may have consisted of doming related to an embryonic stage of the later Late Jurassic
 586 to Early Cretaceous Bay of Biscay and North Atlantic opening, which caused fast-rate basin
 587 tectonic subsidence and an increment in the normal displacement along some previous normal
 588 faults. Nevertheless, the total amount of extension in the study area is small about 13%. Finally, a
 589 N-S to NNW-SSE contractional event, probably related mainly to the Cenozoic Alpine convergence
 590 between the Iberian and Eurasian plates, which caused the Pyrenean and Cantabrian ranges plus the
 591 partial closure of the Bay of Biscay, was responsible for a mild and irregularly distributed basin
 592 inversion which reached about 3% shortening. As a result, previous normal faults were selectively
 593 reactivated as reverse and/or NW-SE right- and NE-SW left-lateral strike-slip faults, offset by
 594 contractional faults, deformed by contractional folds and/or affected by buttressing, and new
 595 approximately E-W reverse faults and folds, some of them related to thrusts, were generated.

Deciphering the main features, relationships and relative timing of the structures in the best exposed portions of the Asturian Basin, such as the cliffs within the study area, may assist with the geological mapping of less well exposed inland parts of the basin and with the geological interpretation of the commercial seismic data acquired by the oil industry in the offshore portion of the basin (e.g., Riaza Molina, 1996). Furthermore, given that some Jurassic beds in the study area have been considered hydrocarbon source rocks because they exhibit high concentrations of organic matter and occasionally have provided bitumen inside brachiopod shells, joints and septarian concretions (e.g., Valenzuela, 1988), understanding their structural configuration may serve as an analogue for unconventional hydrocarbon plays.

Acknowledgements

We would like to thank the editor Cees Passchier and the reviewers Rick Groshong and an anonymous reviewer for their constructive comments and suggestions. We thank Beatriz González Fernández and Eduardo Menéndez Casares for the support provided when mapping the Jurassic rocks. José Graciano Antuña is thanked for maintaining the software and hardware used for data analysis. The authors would like to acknowledge financial support by research projects CGL 2011-23628 (Desarrollo de fracturas y venas asociadas al plegamiento -FRAVEPLE-), CGL2015-66997-R (Aplicación del análisis del plegamiento a la investigación de recursos geológicos -AAPLIREGE-) and CSD 2006-0041 (Geociencias en Iberia: estudios integrados de topografía y evolución 4D - TOPO-IBERIA-) funded by diverse Spanish Ministries and the European Fund for Regional Development (FEDER). H. Uzcheda thanks the support by the Spanish Ministry of Education via an FPU grant partially funded by the European Social Fund. We dedicate this article to the memory of our deceased colleague Andrés Pérez Estaún.

620 **References**

- 621 Allen, P.A., Allen, J.R., 2013. Basin Analysis. Principles and Application to Petroleum Play
622 Assessment. John Wiley & Sons, Chichester, 642 p.
- 623 Alonso, J.L., Gallastegui, J., García-Ramos, J.C., Poblet, J., 2009. Estructuras mesozoicas y
624 cenozoicas relacionadas con la apertura y cierre parcial del Golfo de Vizcaya (Zona Cantábrica –
625 Asturias). Guía de campo del “6º Simposio sobre el Margen Ibérico Atlántico”, Oviedo, 18 p.
- 626 Alonso, J.L., Pulgar, F.J., García-Ramos, J.C., Barba, P., 1996. Tertiary basins and Alpine tectonics
627 in the Cantabrian Mountains. *In*: Friend, P.F., Dabrio, C.J. (Eds.), Tertiary basins of Spain: the
628 stratigraphic record of crustal kinematics. Cambridge University Press, Cambridge, 214-227.
- 629 Álvarez-Marrón, J., Hetzel, R., Niedennann, S., Menéndez, R., Marquínez, J., 2008. Origin,
630 structure and exposure history of a wave-cut platform more than 1 Ma in age at the coast of
631 northern Spain: A multiple cosmogenic nuclide approach. *Geomorphology* 93, 316-334.
- 632 Arenas, C., Piñuela, L., García-Ramos, J.C., 2015. Climatic and tectonic controls on carbonate
633 deposition in syn-rift siliciclastic fluvial systems: A case of microbialites and associated facies in
634 the Late Jurassic. *Sedimentology* 62, 1149-1183.
- 635 Aurell, M., Meléndez, G., Olóriz, F. (coords.), Bádenas, B., Caracuel, J., García-Ramos, J.C., Goy,
636 A., Linares, A., Quesada, S., Robles, S., Rodríguez-Tovar, F.J., Rosales, I., Sandoval, J., Suárez de
637 Centi, C., Tavera, J.M., Valenzuela, M., 2002. Jurassic. *In*: Gibbons, W., Moreno, T. (Eds.), The
638 Geology of Spain. The Geological Society, London, 213-253.
- 639 Aurell, M., Robles, S., Rosales, I., Quesada, S., Meléndez, A., Bádenas, B., García-Ramos, J.C.,
640 2003. Transgressive/regressive cycles and Jurassic paleogeography of northeast Iberia. *Sedimentary*
641 *Geology* 162(3-4), 239-271.

- 642 Bádenas, B., Aurell, M., Armendáriz, M., Rosales, I., García-Ramos, J.C., Piñuela, L., 2012.
 643 Sedimentary and chronostratigraphic record of climatic cycles in Lower Pliensbachian marl
 644 limestone platform successions of Asturias (North Spain). *Sedimentary Geology* 281, 119–138.
- 645 Bádenas, B., Armendáriz, M., Rosales, I., Aurell, M., Piñuela, L., García-Ramos, J.C., 2013. Origen
 646 de los black shales del Pliensbachense inferior de la Cuenca Asturiana (España). *Revista de la*
 647 *Sociedad Geológica de España* 26 (1), 41-54.
- 648 Barrón, E., Gómez, J.J., Goy, A., 2002. Los materiales del tránsito Triásico-Jurásico en la región de
 649 Villaviciosa (Asturias, España). Caracterización palinológica. *Geogaceta* 31, 197-200.
- 650 Barrón, E., Gómez, J.J., Goy, A., Pieren, A.P., 2006. The Triassic-Jurassic boundary in Asturias
 651 (northern Spain): Palynological characterisation and facies. *Review of Palaeobotany and*
 652 *Palynology* 138(3-4), 187-208.
- 653 Beroiz, C., Barón, A., Ramírez del Pozo, J., Giannini, G., Gervilla, M., 1972a. Mapa Geológico de
 654 España, Escala 1:50.000. Hoja 30 (Villaviciosa). Instituto Geológico y Minero de España, Madrid.
- 655 Beroiz, C., Pignatelli, R., Felgueroso, C., Ramírez del Pozo, J., Giannini, G., Gervilla, M., 1972b.
 656 Mapa Geológico de España, Escala 1:50.000. Hoja 29 (Oviedo). Instituto Geológico y Minero de
 657 España, Madrid.
- 658 Boillot, G., Capdevila, R., 1977. The Pyrenees: Subduction and collision? *Earth and Planetary*
 659 *Sciences Letters* 35, 151–160.
- 660 Borrego, A.G., Hagemann, H.V., Blanco, C.G., Valenzuela, M., Suárez de Centi, C., 1997. The
 661 Pliensbachian (Early Jurassic) “anoxic” event in Asturias, northern Spain: Santa Mera Member,
 662 Rodiles Formation. *Organic Geochemistry* 25, 295–309.
- 663 Cadenas, P., 2013. Estructura geológica y modelización tridimensional de la Plataforma Continental
 664 Noribérica entre 4° y 5°30'W (Golfo de Vizcaya). MSc. thesis, Universidad de Oviedo, 47 p.

- 665 Campón, E., Fernández, C.J., Solans Huguet, J., 1978. El azabache de los yacimientos de Oles
666 (Asturias). *Trabajos de Geología* 10, 161-166.
- 667 Carcavilla, L., Piñuela, L., García-Ramos, J.C., Delvene, G., Ruiz-Omeñaca, J.I., 2010.
668 Incorporación de los yacimientos con huellas de dinosaurios del Jurásico asturiano (N España) en el
669 inventario Global Geosites. Comunicaciones del V Congreso del Jurásico de España, Colunga, 170-
670 177.
- 671 Comas-Rengifo, M.J., Goy, A., 2010. Caracterización biocronoestratigráfica del Sinemuriense
672 Superior y el Pliensbachense entre los afloramientos de la Playa Vega y Lastres (Asturias). *In*:
673 García-Ramos, J.C. (coord.), Las sucesiones margo-calcáreas marinas del Jurásico Inferior y las
674 series fluviales del Jurásico Superior. Acantilados de la playa de Vega (Ribadesella). Guía de la
675 excursión A del V Congreso del Jurásico de España, Colunga, 10–18.
- 676 Delvene, G., Munt, M., Piñuela, L., García-Ramos, J.C., 2016. New Unionida (Bivalvia) from the
677 Kimmeridgian (Late Jurassic) of Asturias, Spain, and their palaeobiogeographical implications.
678 *Papers in Palaeontology* 2(1), 1-21.
- 679 Dubar, G., Mousterde, R., 1957. Extension du Kimméridgien marin dans les Asturies depuis
680 Ribadesella jusqu'à Gijón. *Comptes Rendus Hebdomadaires des Séances de l'Académie des*
681 *Sciences* 244(1), 99-101.
- 682 Fernández, O., Muñoz, J.A., Arbués, P., Falivene, O., Marzo, M., 2004. Three-dimensional
683 reconstruction of geological surfaces: An example of growth strata and turbidite systems from the
684 Ainsa basin (Pyrenees, Spain). *AAPG Bulletin* 88(8), 1049-1068.
- 685 Fernández-López, S., Suárez Vega, L.C., 1981. Estudio bioestratigráfico (Ammonoidea) del
686 Aalenense y Bajociense en Asturias. *Estudios Geológicos* 35(1-6), 231-239.
- 687 Flor, G., 1983. Las rasas asturianas; ensayos de correlación y emplazamiento. *Trabajos de Geología*
688 13, 65-81.

- 689 Fürsich, F.T., Werner, W., Delvene, G., García-Ramos, J.C., Bermúdez-Rochas, D.D., Piñuela, L.,
 690 2012. Taphonomy and palaeoecology of high-stress benthic associations from the Upper Jurassic of
 691 Asturias, northern Spain. *Palaeogeography, Palaeoclimatology, Palaeoecology* 358–360, 1-18.
- 692 García-Ramos, J.C., 1997. La sucesión jurásica de la Cuenca Asturiana: entorno paleogeográfico
 693 regional y relaciones tectónica-sedimentación. Comunicaciones del IV Congreso del Jurásico de
 694 España, Alcañiz, 13-14.
- 695 García-Ramos, J.C., 2013. El Jurásico de la costa centro-oriental de Asturias. Un Monumento
 696 Natural de alto interés patrimonial. *Geo-Temas* 14, 19-29.
- 697 García-Ramos, J.C., Gutiérrez Claverol, M., 1995. La cobertera mesozoico-terciaria. In: Aramburu,
 698 C., Bastida, F. (Eds.), Geología de Asturias. Ediciones Trea, Gijón, 81-94.
- 699 García-Ramos, J.C., Piñuela, L., Aramburu, C., 2010b. La Formación Tereñes en su localidad tipo.
 700 In: García-Ramos, J.C., Aramburu, C. (coords.), Las sucesiones litorales y marinas restringidas del
 701 Jurásico Superior. Acantilados de Tereñes (Ribadesella) y de la playa de La Griega (Colunga). Guía
 702 de la excursión B del V Congreso del Jurásico de España, Colunga, 15-40.
- 703 García-Ramos, J.C., Piñuela, L., Aramburu, C., Suárez-Ruiz, I., Ruiz-Omeñaca, J.I., 2008. Asturian
 704 Jurassic Coast. Field Trip Guidebook of the International Conference on Coal and Organic
 705 Petrology, Oviedo, 44 p.
- 706 García-Ramos, J.C., Piñuela, L., Lires, J.F., 2006. Atlas del Jurásico de Asturias. Ediciones Nobel,
 707 Oviedo, 225 p.
- 708 García-Ramos, J.C., Piñuela, L., Rodríguez-Tovar, F.J., 2011. Post-workshop field trip guide. XI
 709 International Ichnofabric Workshop, Colunga, 89 p.
- 710 García-Ramos, J.C., Piñuela, L., Uzcheda, H., Poblet, J., Bulnes, M., Alonso, J.L., Suárez Vega,
 711 L.C., 2010a. Travertinos ricos en oncoides asociados a paleomanantiales y lagos efímeros próximos

- 712 a fallas sinsedimentarias en el Jurásico Superior de Asturias. Comunicaciones del V Congreso del
713 Jurásico de España. Colunga, 83-91.
- 714 García-Ramos, J.C., Suárez de Centi, C., Valenzuela, M., 1992. Icnofósiles, sedimentación
715 episódica, tempestitas fangosas y “black shales” de ambientes pseudoanóxicos, en sucesiones
716 marinas de plataforma y rampa. *Geogaceta* 12, 99-100.
- 717 González, B., Menéndez Casares, E., García-Ramos, J.C., 2004. Subunidades litoestratigráficas de
718 la Formación Gijón (Triásico Superior–Jurásico Inferior) en Asturias. *Geo-Temas* 6, 71–74.
- 719 Goy, A., Comas-Rengifo, M.J., Gómez, J.J., Herrero, C., Suárez-Vega, L.C., Ureta, S., 2010.
720 Biohorizontes de ammonioideos del Toarciense en Asturias. Comunicaciones del V Congreso del
721 Jurásico de España, Colunga, 94-95.
- 722 Gutierrez, K., Sheldon, N.D., 2012. Paleoenvironmental reconstruction of Jurassic dinosaur habitats
723 of the Vega Formation, Asturias, Spain. *GSA Bulletin* 124, 596–610.
- 724 Gutiérrez Claverol, M., López-Fernández, C., Alonso, J.L., 2006. Procesos neotectónicos en los
725 depósitos de rasa en la zona de Canero (Occidente de Asturias). *Geogaceta* 40, 75-78.
- 726 Gutiérrez Claverol, M., Pando, L., García-Ramos, J.C., 2008. Procesos y productos de alteración de
727 formaciones rocosas en Asturias y su repercusión socio-económica. *Boletín Geológico y Minero*
728 119(2), 211-230.
- 729 Hallam, A., 1988. A re-evaluation of Jurassic eustasy in the light of new data and the revised Exxon
730 curve. In: Wilgus, C.K., Hastings, B.S., Kendall, C.G.St.C., Posamentier, H.W., Ron, C.A., van
731 Wagner, J.C. (Eds.), Sea-Level Changes – An Integrated Approach. SEPM Special Publication 42,
732 261-273.
- 733 Haq, B.U., Hardenbol, J., Vail, P.R., 1987. Chronology of fluctuating sea levels since the Triassic
734 (250 million years ago to present). *Science* 235(4793), 1156-1167.

- 735 International Commission on Stratigraphy 2015. International Chronostratigraphic Chart v2015/01.
736 <http://www.stratigraphy.org/ICSchart/ChronostratChart2015-01.pdf>.
- 737 Julivert, M., Fontboté, J. M., Ribeiro, A., Conde, L. E., 1972. Mapa Tectónico de la Península
738 Ibérica y Baleares, escala 1: 1000000. Instituto Geológico y Minero de España, Madrid.
- 739 Julivert, M., Ramírez del Pozo, J., Truyols, J., 1971. Le réseau de failles et la couverture post-
740 Hercynienne dans les Asturies. *In: Histoire structural du Golfe de Gascogne*, vol. 1, Publications de
741 l'Institut Français du Pétrole, Editions Technip, Paris, 3-1 to 3-33.
- 742 Kamb, W.B., 1959. Ice petrofabric observations from Blue Glacier, Washington in relation to
743 theory and experiment. *Journal of Geophysical Research* 64, 1891-1909.
- 744 Le Pichon, X., Sibuet, J.C., 1971. Western extension of boundary between European and Iberian
745 plates during the Pyrenean orogeny. *Earth and Planetary Science Letters* 12(1), 83-88.
- 746 Lepvrier, C., Martínez-García, E., 1990. Fault development and stress evolution of the post-
747 Hercynian Asturian basin (Asturias and Cantabria, northwestern Spain). *Tectonophysics* 184, 345-
748 356.
- 749 Lockley, M.G., Lires, J., García-Ramos, J.C., Piñuela, L., Avanzini, M., 2007. Shrinking the
750 world's largest dinosaur tracks: Observations on the ichnotaxonomy of *Gigantosauropus asturiensis*
751 and *Hispanosauropus hauboldi* from the Upper Jurassic of Asturias. *Ichnos* 14(3-4), 247-255.
- 752 López-Fernández, C., Pulgar, J.A., González-Cortina, J.M., Gallart, J., Díaz, J., Ruiz, M., 2004.
753 Actividad Sísmica en el NO de la Península Ibérica observada por la red sísmica local del Proyecto
754 GASPI. *Trabajos de Geología* 24, 91-106.
- 755 Lotze, F., 1945. Zur gliederung der varisziden der Iberischen Meseta. *Geotektonische Forschungen*
756 6, 78-92.

- 757 Lozano, R., Delvene, G., M., Piñuela, L., García-Ramos, J.C., 2016. Late Jurassic biogeochemical
758 microenvironments associated with microbialite-coated unionids (Bivalvia), Asturias (N Spain).
759 *Palaeogeography, Palaeoclimatology, Palaeoecology* 443, 80–97.
- 760 Marrett, R., Allmendinger, R.W., 1990. Kinematic analysis of fault-slip data. *Journal of Structural*
761 *Geology* 12(8), 973-986.
- 762 Martín, S., Uzcheda, H., Poblet, J., Bulnes, M., Rubio, R., 2013. Construction of accurate geological
763 cross-sections along trenches, cliffs and mountain slopes using photogrammetry. *Computers &*
764 *Geosciences* 51, 90-100.
- 765 Mary, G., 1983. Evolución del margen costero de la Cordillera Cantábrica en Asturias desde el
766 Mioceno. *Trabajos de Geología* 13, 3-35.
- 767 Menéndez Casares, E., González Fernández, B., Gutiérrez Claverol, M., García-Ramos, J.C., 2004.
768 Precisiones sobre los acuíferos de la cuenca jurásica asturiana (NO de España). *Trabajos de*
769 *Geología* 24, 119-126.
- 770 Olóriz, F., Valenzuela, M., García-Ramos, J.C., Suárez de Centi, C., 1988. The first record of the
771 genus *Eurasenia* (Ammonitina) from the Upper Jurassic of Asturias (northern Spain). *Geobios*
772 21(6), 741-748.
- 773 Pignatelli, R., Giannini, G., Ramírez del Pozo, J., Beroiz, C., Barón, A., 1972. Mapa Geológico de
774 España escala 1:50 000, Hoja 15 (Lastres). Instituto Geológico y Minero de España, Madrid.
- 775 Pujalte, V., Robles, S., García-Ramos, J.C., Hernandez, J.M., 2004. El Malm-Barremiense no
776 marino de la Cordillera Cantábrica. In: Vera, J.A. (Ed.), *Geología de España*, Sociedad Geológica
777 de España-Instituto Geológico y Minero de España, Madrid, 288-291.
- 778 Pulgar, J.A., Alonso, J.L., Espina, R.G., Marín, J.A., 1999. La deformación alpina en el basamento
779 varisco de la Zona Cantábrica. *Trabajos de Geología* 21, 283-294.

- 780 Riaza Molina, C., 1996. Inversión estructural en la cuenca mesozoica del off-shore asturiano.
- 781 Revisión de un modelo exploratorio. *Geogaceta* 20(1), 169-171.
- 782 Robles, S., Quesada, S., Rosales, I., Aurell, M., García-Ramos, J.C., 2004. El Jurásico marino de la
- 783 Cordillera Cantábrica. In: Vera, J.A. (Ed.), Geología de España. Sociedad Geológica de España-
- 784 Instituto Geológico y Minero de España, Madrid, 279-285.
- 785 Ruiz-Omeñaca, J.I., García-Ramos, J.C., Piñuela, L., Bardet, N., Bermúdez-Rochas, D.D., Canudo,
- 786 J.I., Pereda Suberbiola, X., 2006. Restos directos de vertebrados del Jurásico de Asturias. Libro de
- 787 resúmenes de las XXII Jornadas de la Sociedad Española de Paleontología y simposios de los
- 788 proyectos PICG 493, 503, 499 y 467, León, 171-173.
- 789 Salas, R., Casas, A., 1993. Mesozoic extensional tectonics, stratigraphy and crustal evolution during
- 790 the Alpine cycle of the eastern Iberian basin. *Tectonophysics* 228(1-2), 33-55.
- 791 Sánchez, V., Corbella, M., Fuenlabrada, J. M., Vindel, E., Martín-Crespo, T., 2006. Sr and Nd
- 792 isotope data from the fluor spar district of Asturias, northern Spain. *Journal of Geochemical*
- 793 *Exploration* 89(1), 348-350.
- 794 Sánchez, V., Cardellach, E., Corbella, M., Vindel, E., Martín-Crespo, T., Boyce, A. J., 2010.
- 795 Variability in fluid sources in the fluorite deposits from Asturias (N Spain): Further evidences from
- 796 REE, radiogenic (Sr, Sm, Nd) and stable (S, C, O) isotope data. *Ore Geology Reviews* 37(2), 87-
- 797 100.
- 798 Schmoker, J. W., Halley, R. B., 1982. Carbonate porosity versus depth: a predictable relation for
- 799 south Florida. *AAPG Bulletin* 66(12) 2561-2570.
- 800 Schudack, M., Schudack, U. (2002. New biostratigraphical data for the Upper Jurassic of Asturias
- 801 (Northern Spain) based on Ostracoda. *Revista Española de Micropaleontología* 34(1), 1-18.

- 802 Sclater, J. G., Christie, P., 1980. Continental stretching: An explanation of the post-mid-Cretaceous
 803 subsidence of the central North Sea basin. *Journal of Geophysical Research: Solid Earth* (1978–
 804 2012) 85(B7), 3711-3739.
- 805 Soler, R., López Vilchez, J., Riaza Molina, C., 1981. Petroleum geology of the Bay of Biscay. *In*:
 806 Illing, L.V., Hobson, G.D. (Eds.), *Petroleum geology of the Continental shelf of north-west Europe*.
 807 London Institute of Petroleum, 474-482.
- 808 Suárez Rodríguez, A., 1988. Estructura del área de Villaviciosa-Libardón (Asturias, Cordillera
 809 Cantábrica). *Trabajos de Geología* 17, 87-98.
- 810 Suárez-Ruiz, I., 1989. Caracterización, clasificación y estudio de la evolución de la materia
 811 orgánica dispersa (MOD) en el Jurásico de Asturias y Cantabria. PhD thesis, Universidad de
 812 Oviedo, Oviedo, 372 p.
- 813 Suárez-Ruiz, I., Iglesias, M.J., Jiménez, A., Cuesta, M.J., Laggoun-Défarge, F., 2006. El azabache
 814 de Asturias: características físico-químicas, propiedades y génesis. *Trabajos de Geología* 26, 9-18.
- 815 Suárez Ruiz, I., Prado, J.G., 1995. Characterization of Jurassic black shales from Asturias (northern
 816 Spain): evolution and petroleum potential. *In*: Snape, C. (Ed.), *Composition, Geochemistry and*
 817 *Conversion of Oil Shales*. Kluwer Academic Publishers, 387-393.
- 818 Suárez Vega, L.C., 1974. Estratigrafía del Jurásico de Asturias. *Cuadernos de Geología Ibérica*
 819 74(3), 1-369.
- 820 Uzkeda, H., 2013. Reconstrucción 3D y análisis estructural de las rocas jurásicas de Colunga-
 821 Tazones (Cuenca Asturiana, NO de la Península Ibérica). PhD thesis, Universidad de Oviedo,
 822 Oviedo, 244 p.

- 823 Uzkeda, H., Bulnes, M., Poblet, J., García-Ramos, J.C., Piñuela, L., 2013. Buttrressing and reverse
824 reactivation of a normal fault in the Jurassic rocks of the Asturian Basin, NW Iberian Peninsula.
825 *Tectonophysics* 599, 117-134.
- 826 Valenzuela, M., 1988. Estratigrafía, Sedimentología y Paleogeografía del Jurásico de Asturias. PhD
827 thesis, Universidad de Oviedo, Oviedo, 748 p.
- 828 Valenzuela, M., García-Ramos, J.C., Suárez de Centi, C., 1986. The Jurassic sedimentation in
829 Asturias (N Spain). *Trabajos de Geología* 16, 121-132.
- 830 Valenzuela, M., García-Ramos, J.C., Suárez de Centi, C., 1989. La sedimentación en una rampa
831 carbonatada dominada por tempestades, ensayos de correlación de ciclos y eventos en la ritmita
832 margo-calcárea del Jurásico de Asturias. *Cuadernos de Geología Ibérica* 13, 217-235.
- 833 Van Hoorn, B., 1987. The South Celtic Sea/Bristol Channel Basin: origin, deformation and
834 inversion history. *Tectonophysics* 137 (1-4), 309-334.
- 835 Ziegler, P.A., 1989. Geodynamic model for Alpine intra-plate compressional deformation in
836 Western and Central Europe. In: Cooper, M.A., Williams, G.D. (Eds.), *Inversion Tectonics*.
837 Geological Society Special Publications 44, 63-85.

838 **Figure captions**

839 Figure 1. Structural sketch of the Asturian Basin and surrounding areas (modified from Alonso et
840 al., 2009) showing the position of the study area (red rectangle) and the cross section X-X' in figure
841 16b.

842 Figure 2. Stratigraphic column showing the age, lithologies and sedimentary environment of the
843 Jurassic units that crop out in the study area (modified from García-Ramos and Gutiérrez Claverol,
844 1995 based on Valenzuela et al., 1986).

845 Figure 3. Geological map of the studied region showing the location of the cross sections illustrated
846 in figures 6 and 7, and the location of the stations in figure 9.

847 Figure 4. a) View towards the S and b) towards the N of the 3D geological model of the study area
848 constructed using the software Gocad.

849 Figure 5. Weighted rose diagrams for the major a) normal faults and b) reverse faults mapped
850 within the study area that illustrate the orientation of the faults versus their map length in meters.

851 Figure 6. Geological sections A-A', B-B' and C-C' across the eastern portion of the study area. See
852 location in figure 3.

853 Figure 7. Geological sections 1-1' to 4-4' across the whole study area. See location in figure 3.

854 Figure 8. Equal area projections (left) and rose diagrams (right) for: a) normal faults; b) reverse
855 faults; c) right-lateral faults; d) left-lateral faults; e) normal faults reactivated as right-lateral faults;
856 f) normal faults reactivated as left-lateral faults; g) normal faults reactivated as reverse faults; and h)
857 joints. The black circles in the equal area projections and white circles in the rose diagrams
858 correspond to the kinematic indicators.

859 Figure 9. Equal area projections of the folded bedding (black circles) identified in the field,
860 including the fold axes (white circles) as well as the faults nearby (thin black lines). Stations 1 and 2

are located in the northwestern part of the study area, stations 3 and 4 in the northern-middle part, and stations 5 to 19 in the southeastern part. See figure 3 for location of the stations.

Figure 10. Geological photo-interpretations of folds developed on the a) marls of the Tereñes Fm., E of the Lastres Beach (station 5 in figure 9); b) and c) alternations of limestones and marls of the Rodiles Fm., E of La Griega Beach (stations 11, 12 and 18 in figure 9); d) marls of the Tereñes Fm., La Griega Beach (station 8 in figure 9); and e) marls of the Tereñes Fm., E of the Lastres Beach (station 7 in figure 9). f) Simplified geological map of a small region in La Griega Beach (station 8 in figure 9). The scale is approximate.

Figure 11. Field aspect of two sets of joints developed on a bedding surface in the sandstones of the Vega Fm. in the Lastres Beach. The scale is approximate.

Figure 12. Structural sketch of the study area showing the main faults and the position of four stratigraphic columns constructed by Suárez Vega (1974) used to build the 3D geological model depicted in figure 4. In section A-A' the stratigraphic columns called "Rodiles W", located in the footwall of a NE-SW fault, and "Santa Mera NE", located in the hangingwall of the same fault, are compared. In section B-B' we compare the stratigraphic columns called "La Griega E", located in the hangingwall of a NW-SE fault, and "Lastres Beach", located in the footwall of the same fault. The names of the stratigraphic columns correspond to the original ones given by Suárez Vega (1974).

Figure 13. a) Geological interpretation of a photograph mosaic taken from a plane showing the variation in the orientation of the joints (white lines) depending on their position within a decametre-scale fold developed in the Vega Fm. sandstones in the Lastres Beach. b) and c) Geological interpretation of an anticline and a syncline respectively including some faults both developed in the alternations of limestones and marls of the Rodiles Fm. at La Conejera Inlet. The scale is approximate.

Figure 14. Equal area projections including fault planes (thin black lines), their striae (black circles with arrows indicating their displacement sense), kinematic axes (red circles for T axes and blue circles for P axes), extensional (grey regions) and compressive (white regions) stress fields, and orientations of the principal axes (labelled black squares) for the extensional (a to d figures) and contractional (e to g figures) events. a) Projection of all the collected data, b) data from the western part of the study area, c) data from the central part of the study area, d) data from the eastern part of the study area, e) projection of all the collected data, f) data from the western part of the study area and g) data from the eastern part of the study area.

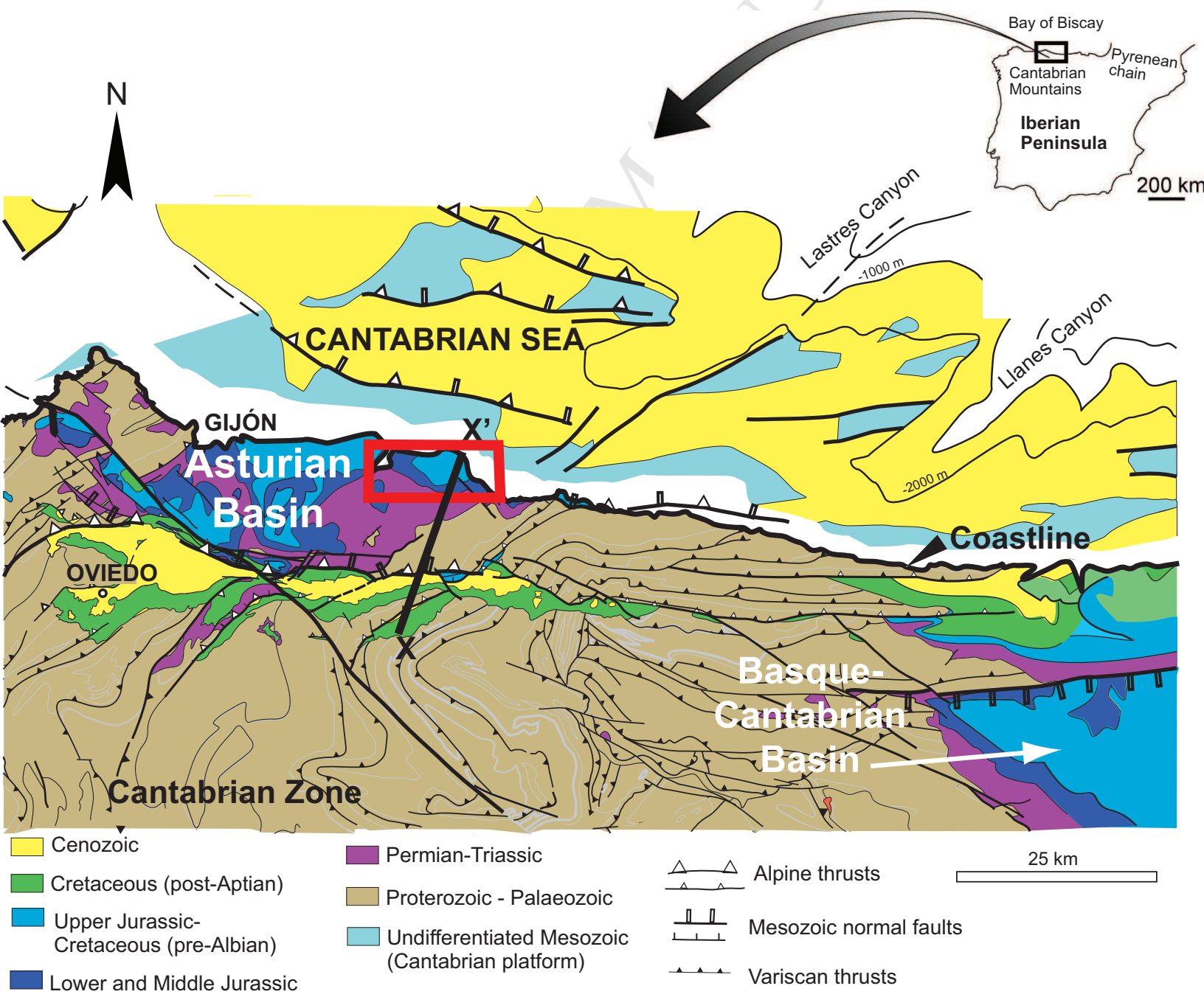
Figure 15. a) Structural sketch of the study area showing the main faults and the position of the stations established to determine the orientation of the tectonic transport vectors shown in b). b) Structural sketch of the study area showing the main faults and folds and the mean tectonic transport directions obtained using local tectonic transport directions from faults and folds. The section line of the geological cross-section I-I' depicted in figure 16a is indicated.

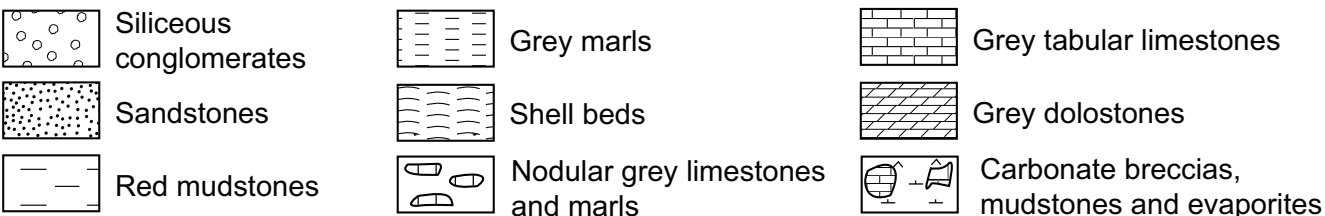
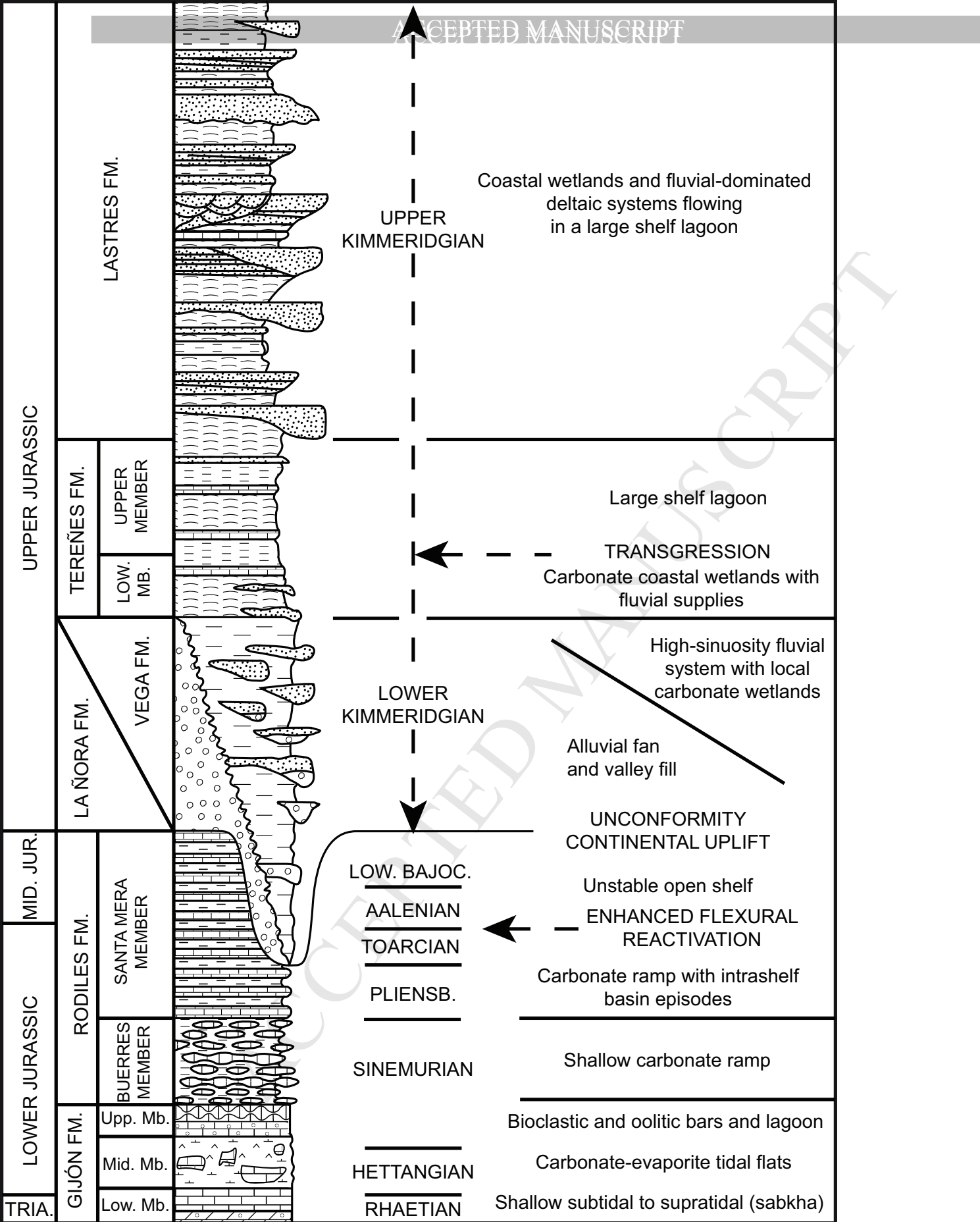
Figure 16. a) Deformed, present-day geological section I-I' across the study area, rotated cross-section and cross sections restored to different stages using the algorithm flexural slip within the software Geosec. See location of the geological cross-section I-I' in figure 15b. b) Regional geological section X-X' across the Asturian Basin resulting from merging the geological section across the study area I-I' depicted in a) (orange rectangle) with geological cross-sections from Beroiz et al. (1972a), Suárez Rodríguez (1988), Alonso et al. (1996) and Pulgar et al. (1999). The lower, filled cross-section shows the complete regional section including the depth to the detachment, whereas the upper, unfilled cross-section is a zoom in of the black square in the lower section showing the regional dip for the Mesozoic beds. See location of the regional cross-section X-X' in figure 1.

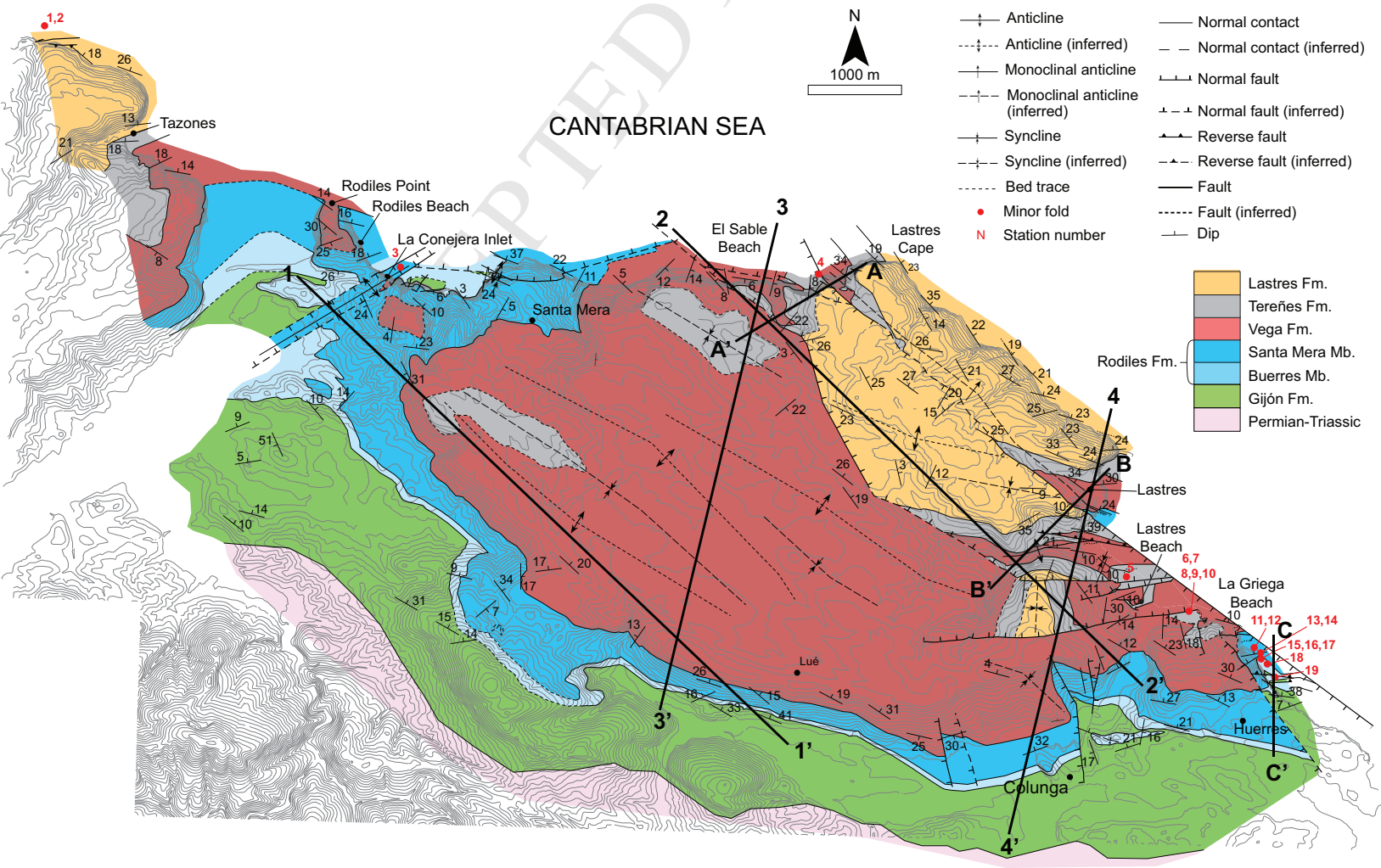
Figure 17. Curves of: a) "total" subsidence and b) "tectonic" subsidence for the study area from Late Triassic to Late Jurassic. The "tectonic" subsidence curve includes error curves. The graph

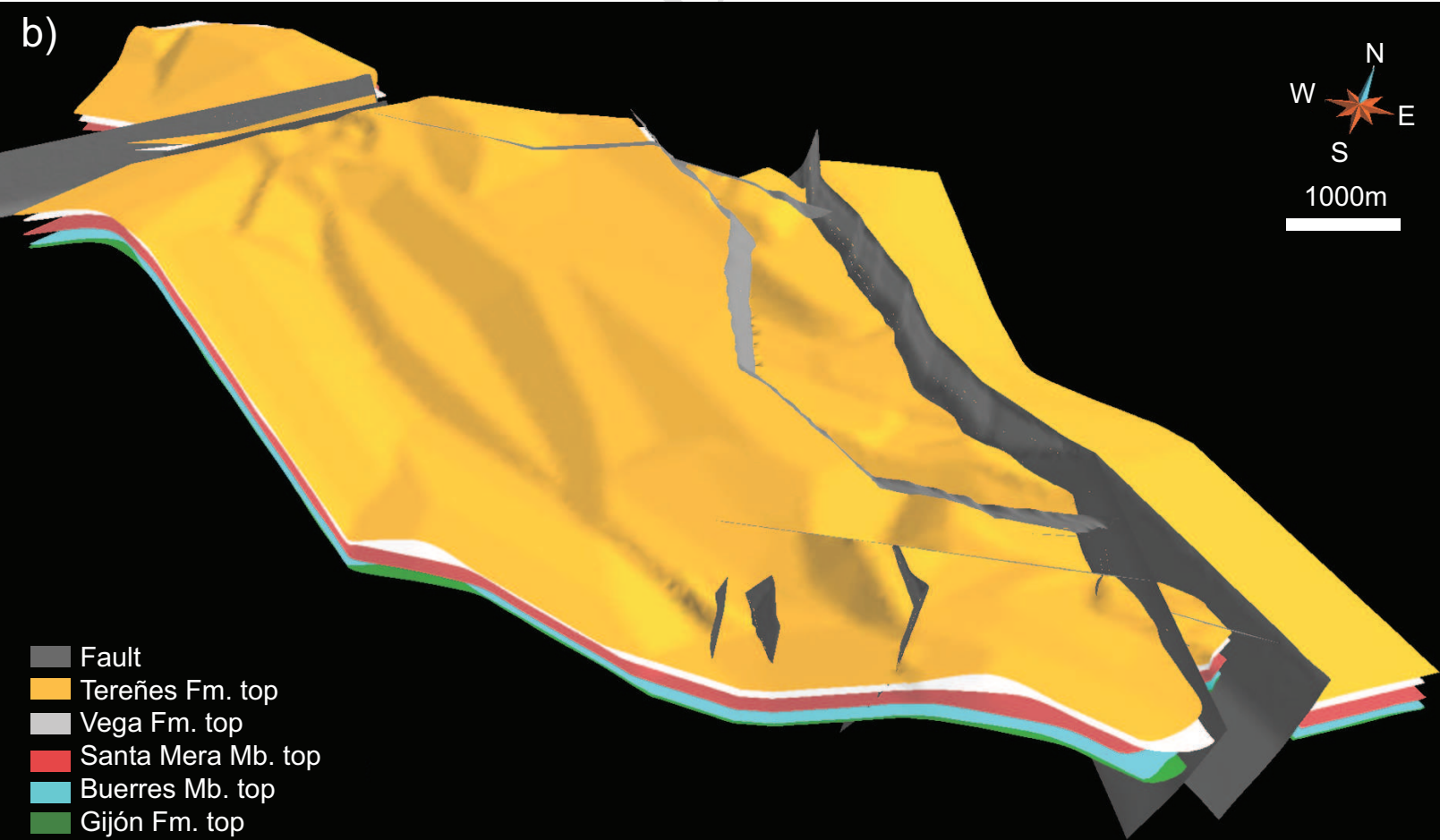
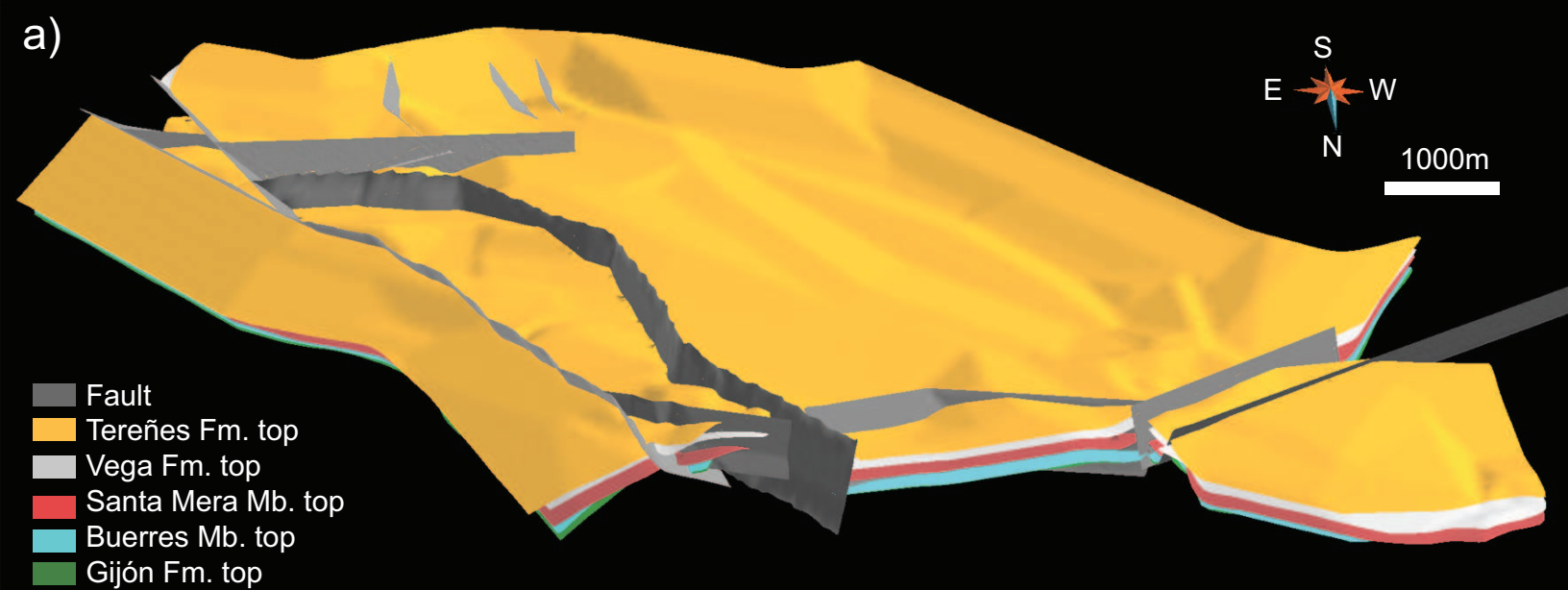
910 depicted in b) includes the climax of thermal flow (data taken from Suárez-Ruiz, 1989) and periods
911 of fault activity indicating the main orientation of the faults. The motion of NE-SW faults after
912 sedimentation of the Vega Fm. and the motion of NW-SE faults during or after sedimentation of the
913 Lastres Fm. have not been displayed in the graph because of the uncertainties in the accurate ages.
914 Curves of global sea level taken from Hallam (1988) (curve 1) and Haq et al. (1987) (curve 2) have
915 been included at the bottom of both figures. Ages based on the International Commission on
916 Stratigraphy (2015).

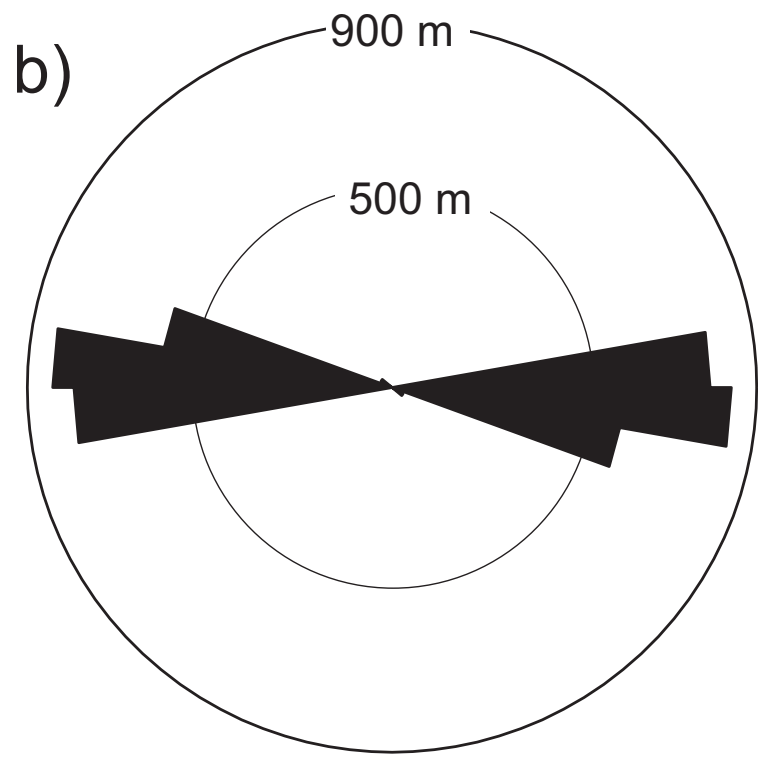
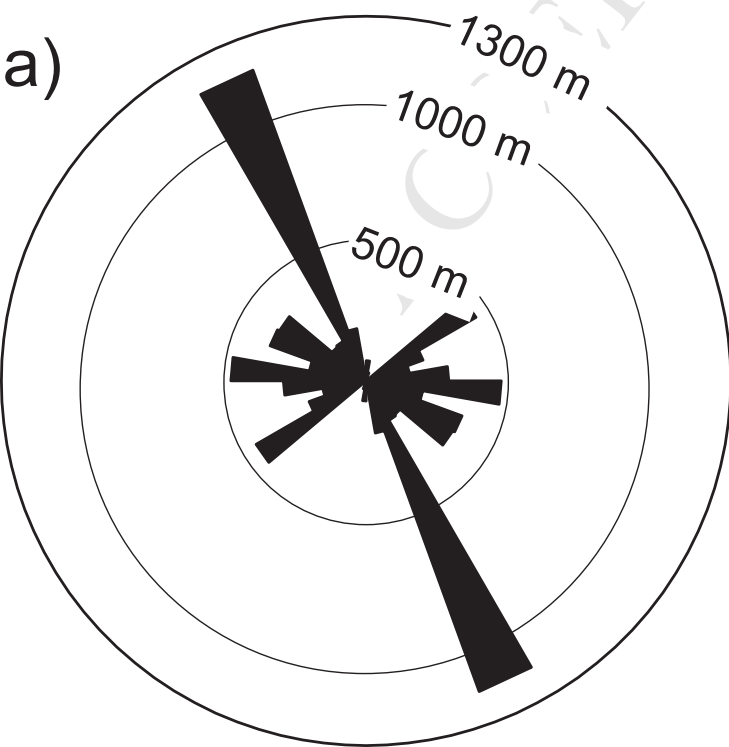
917 Figure 18. Cartoons without scale indicating active and inactive faults at different times depicting
918 the structural evolution of the study area: a) Carboniferous, b) Permian-Triassic, c) Middle
919 Toarcian, d) Late Toarcian, e) Kimmeridgian and f) Cenozoic. The Carboniferous (Variscan) thrusts
920 orientation was taken from Beroiz et al. (1972a, 1972b) and the Permian-Triassic faults orientation
921 was obtained from Suárez Rodríguez (1988) and Lepvrier and Martínez-García (1990).







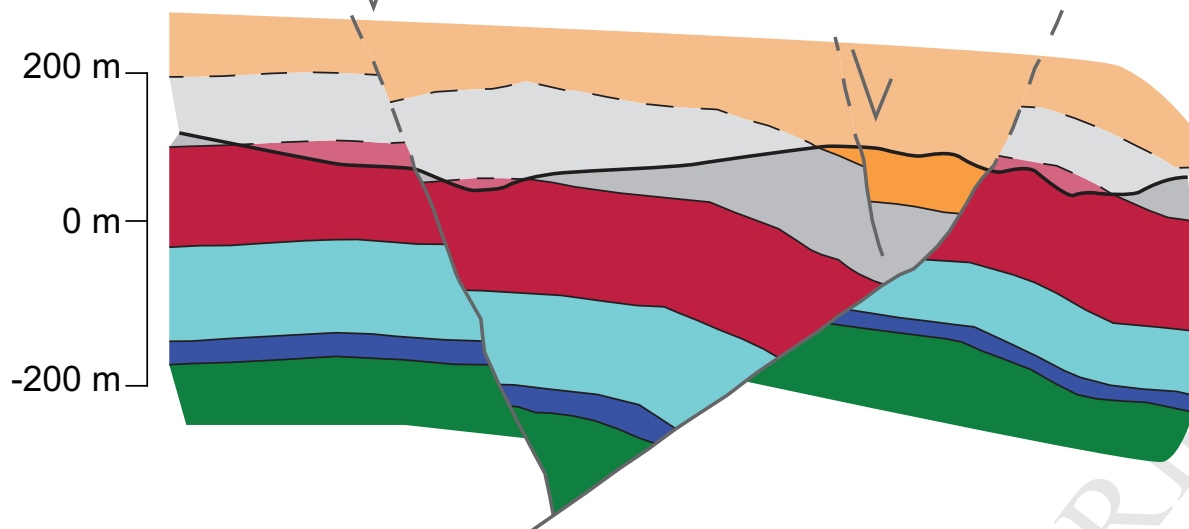




SW (A')

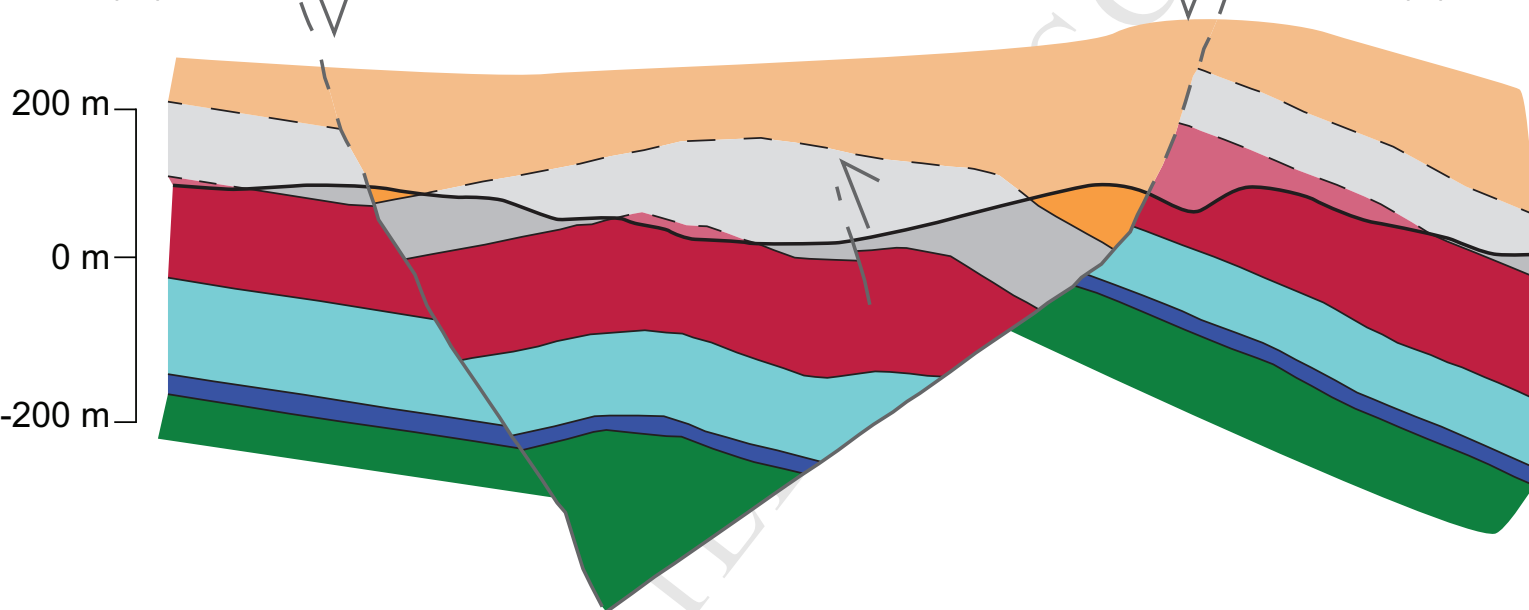
ACCEPTED MANUSCRIPT

(A) NE



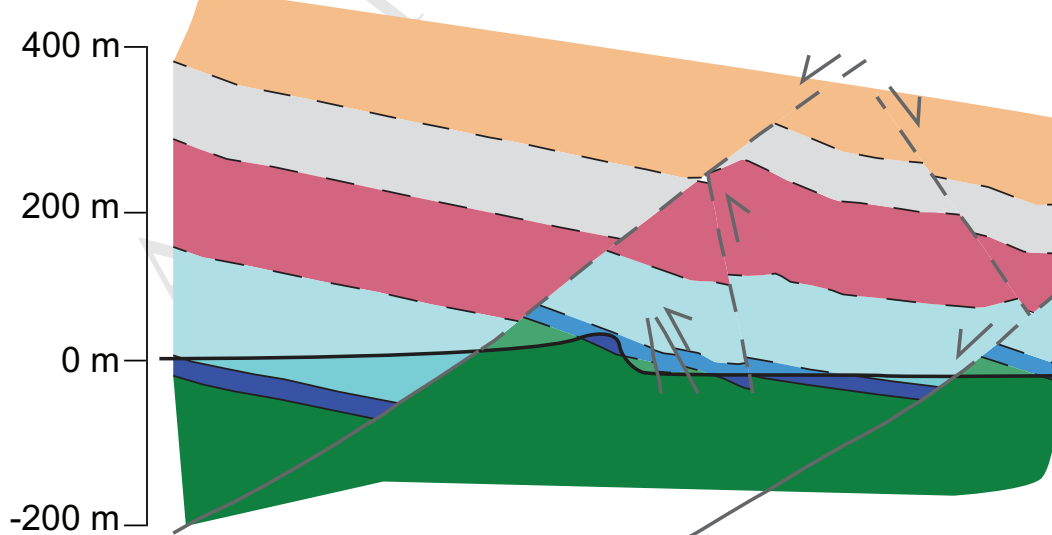
SW (B')

(B) NE



S (C')

(C) N



H=V

200 m

Lastres Fm.

Tereñes Fm.

Topography

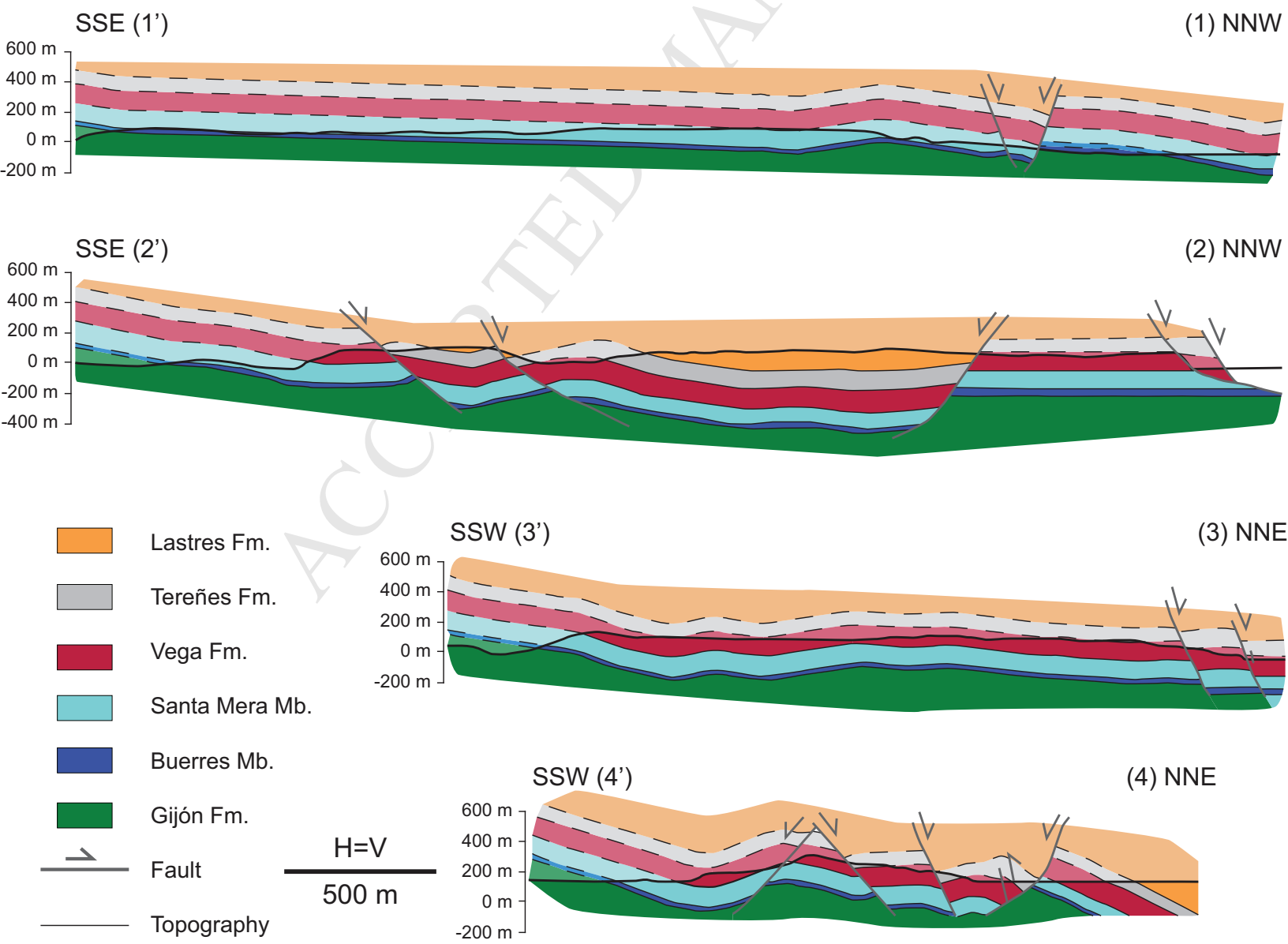
Vega Fm.

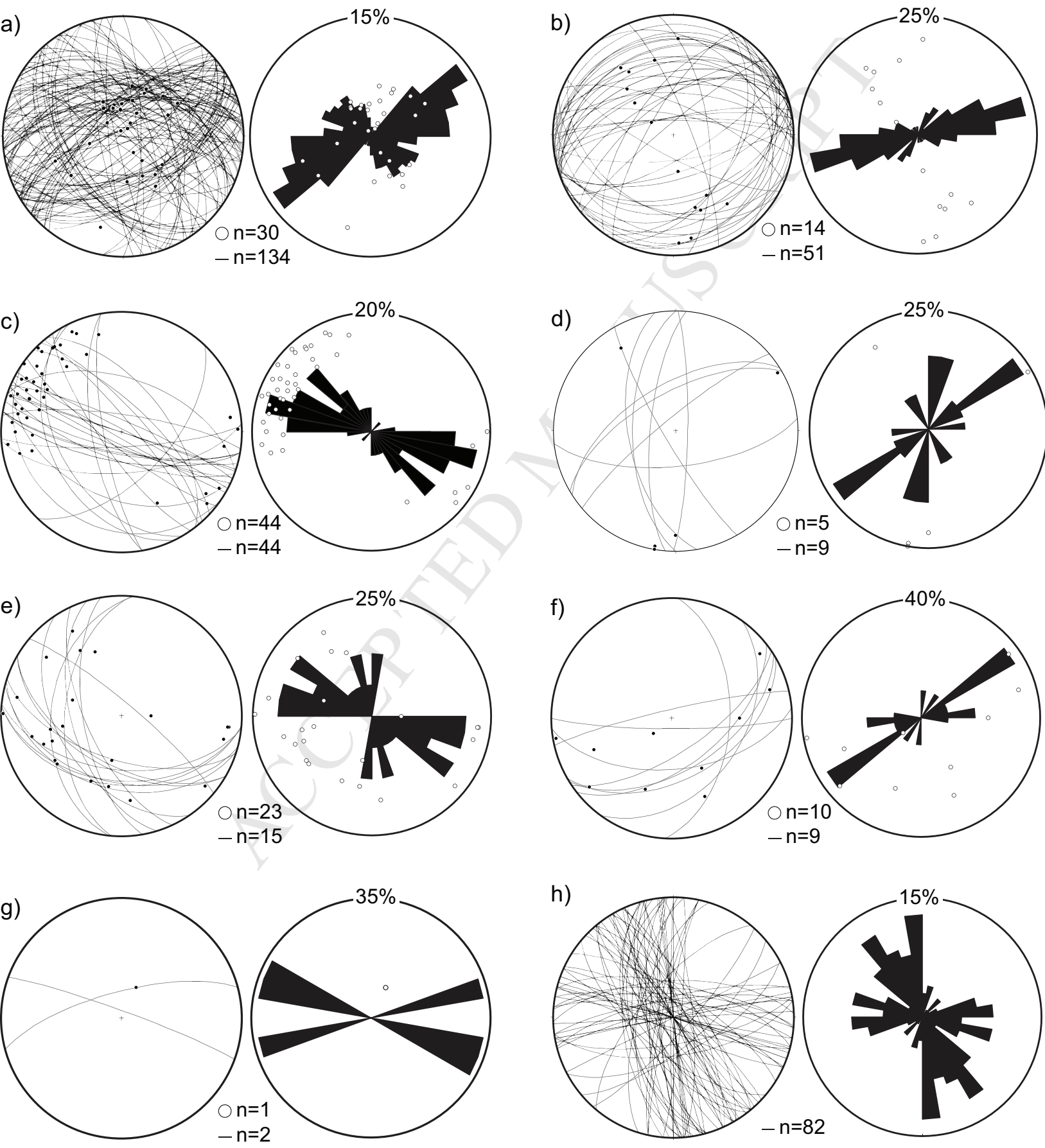
Santa Mera Mb.

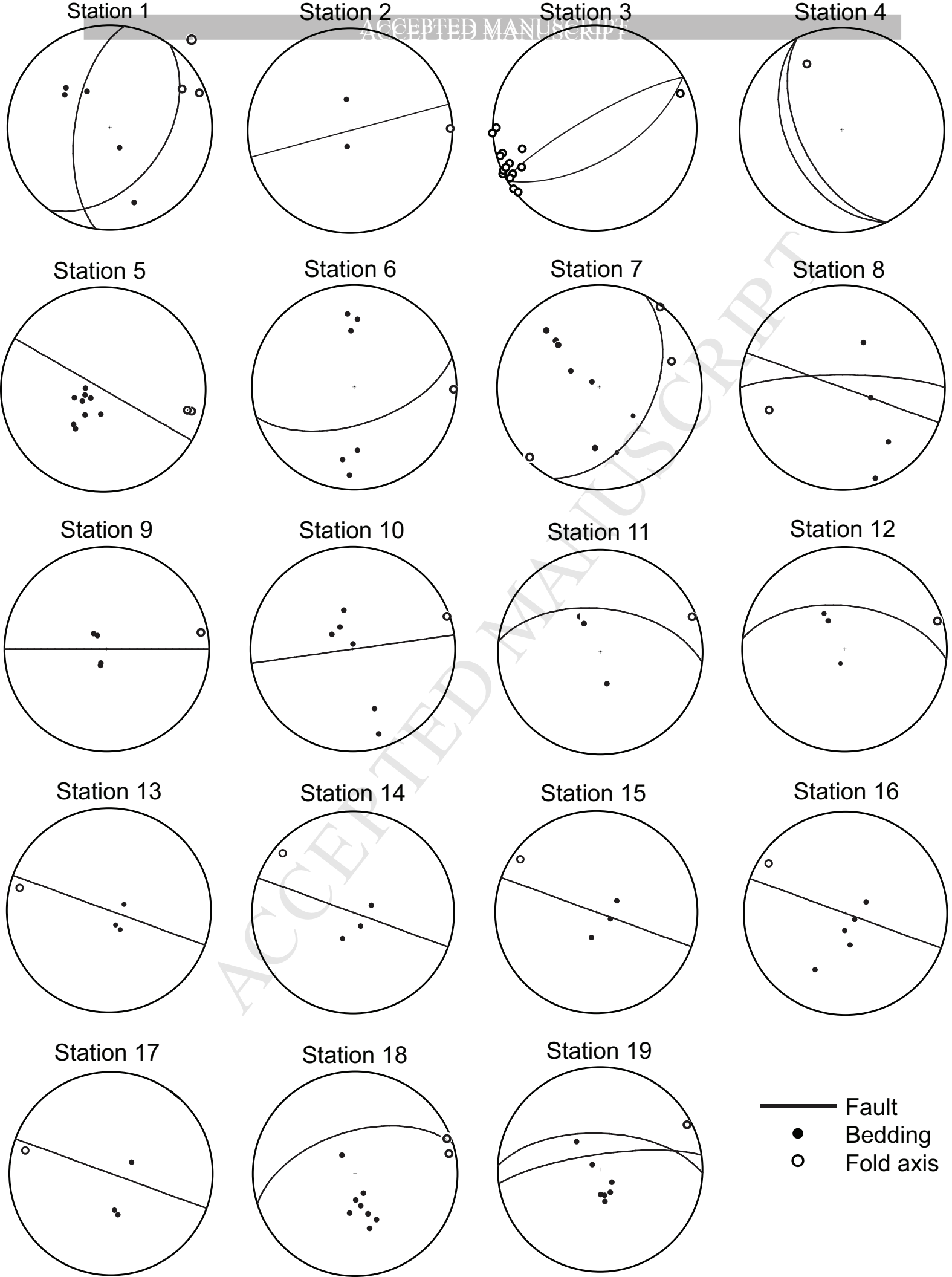
Fault

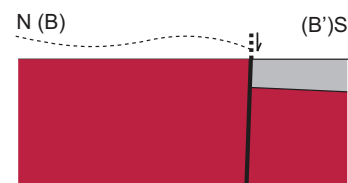
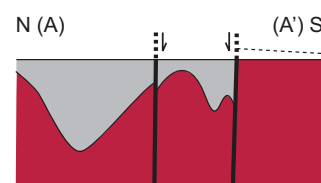
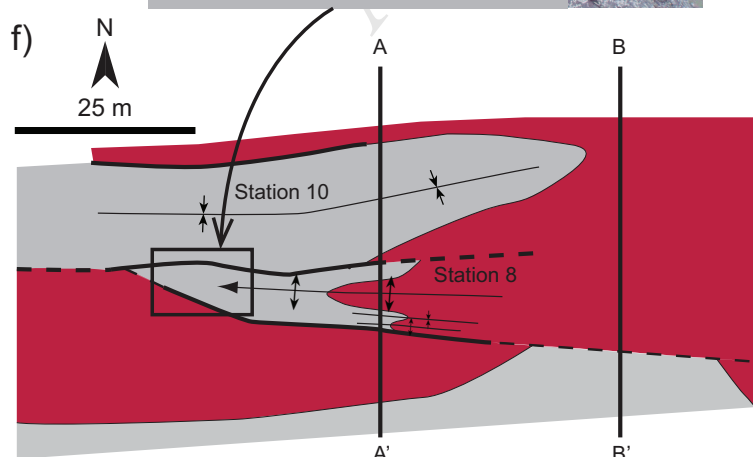
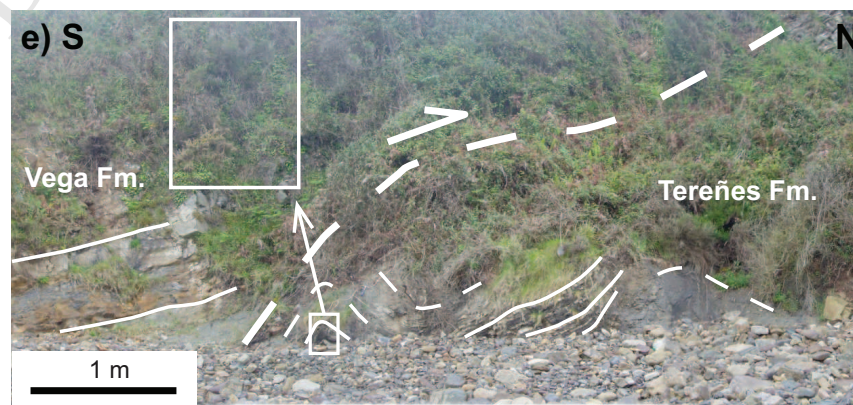
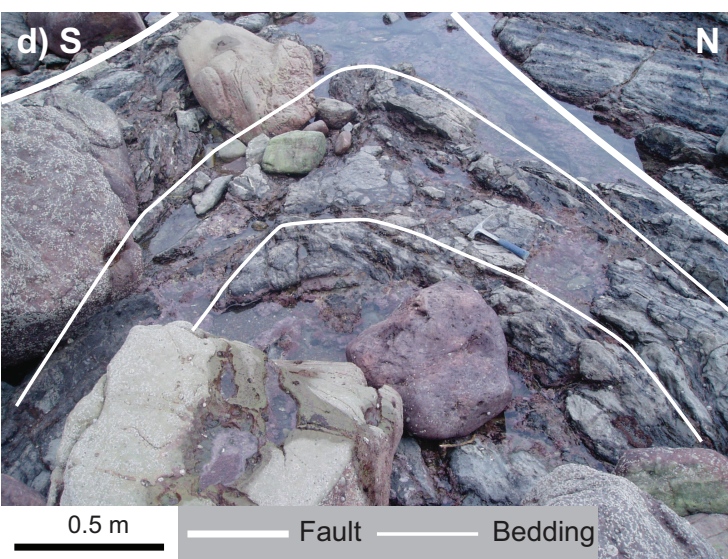
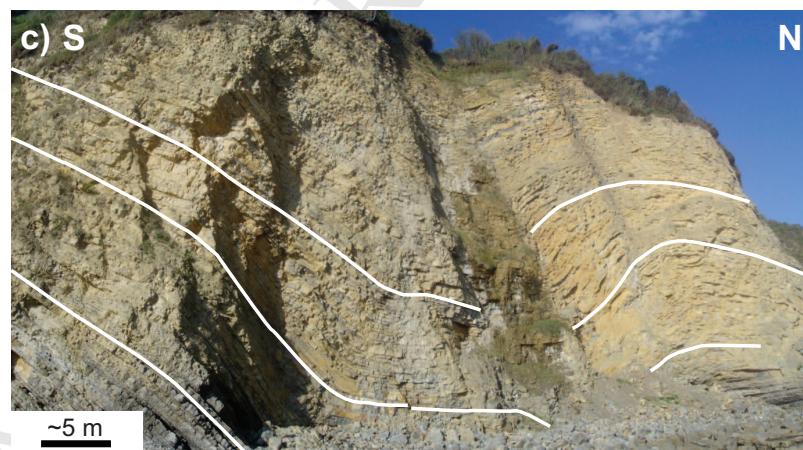
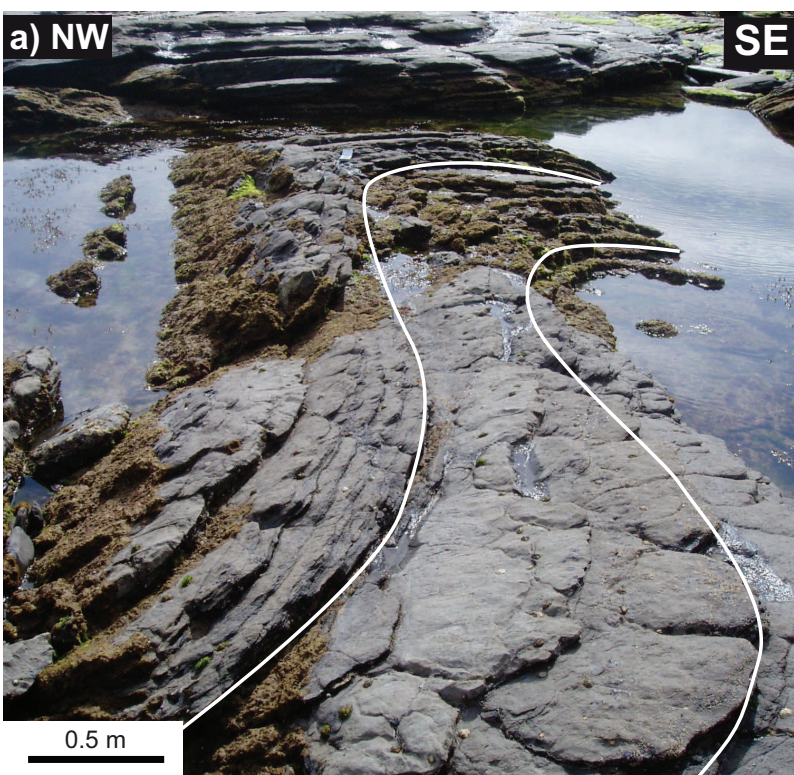
Buerres Mb.

Gijón Fm.

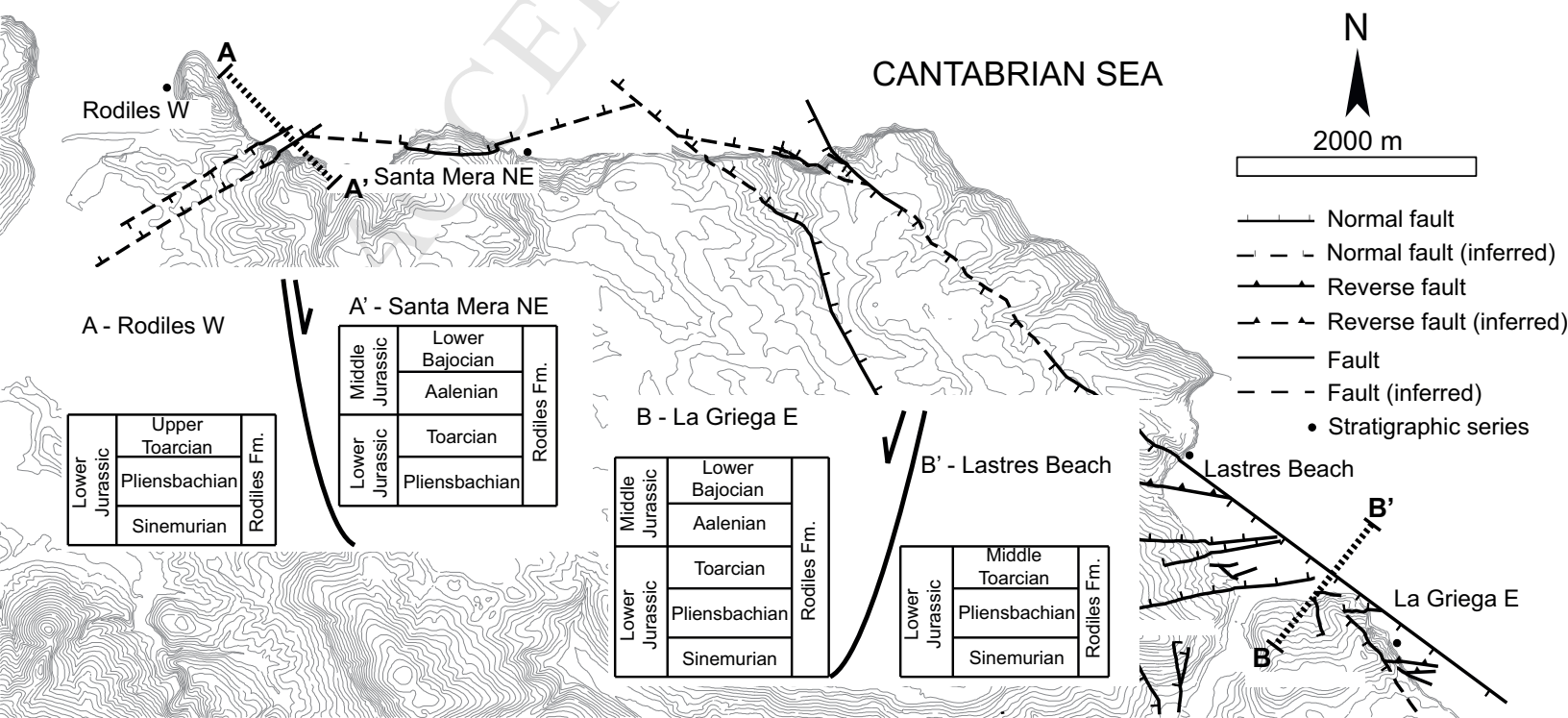


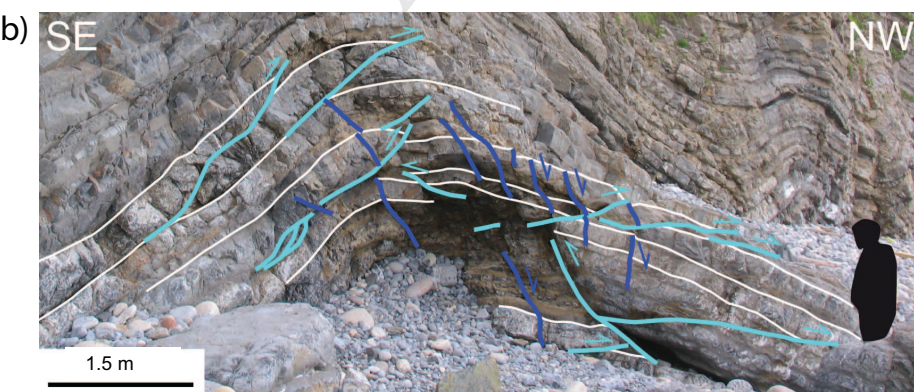
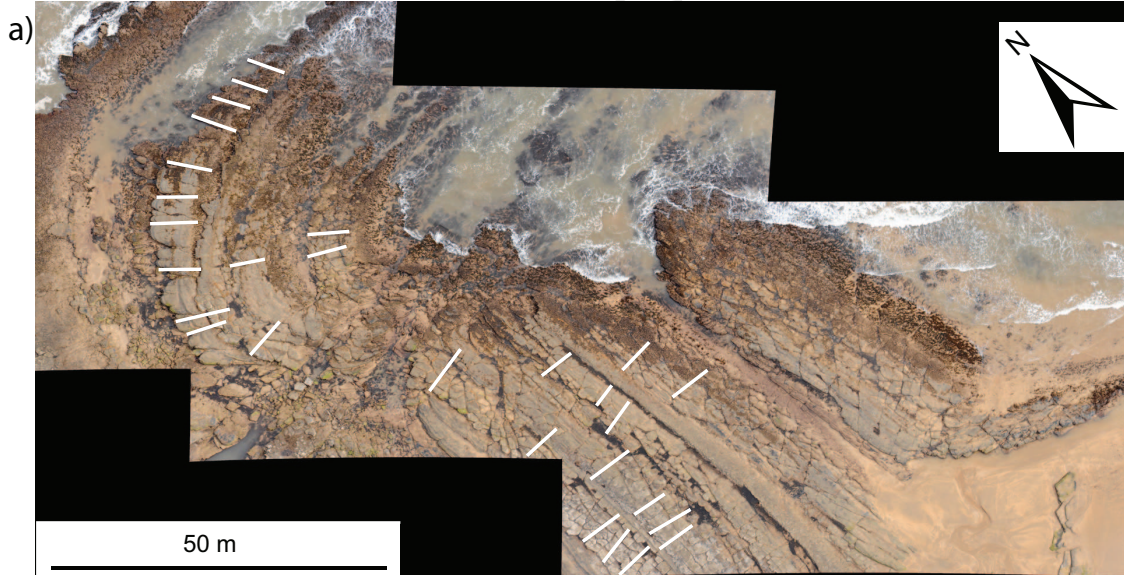




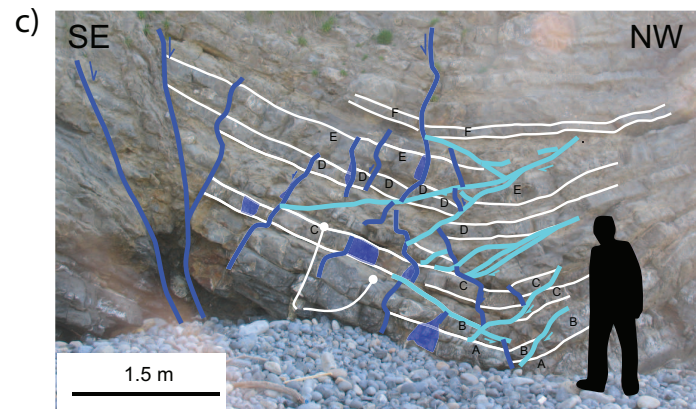


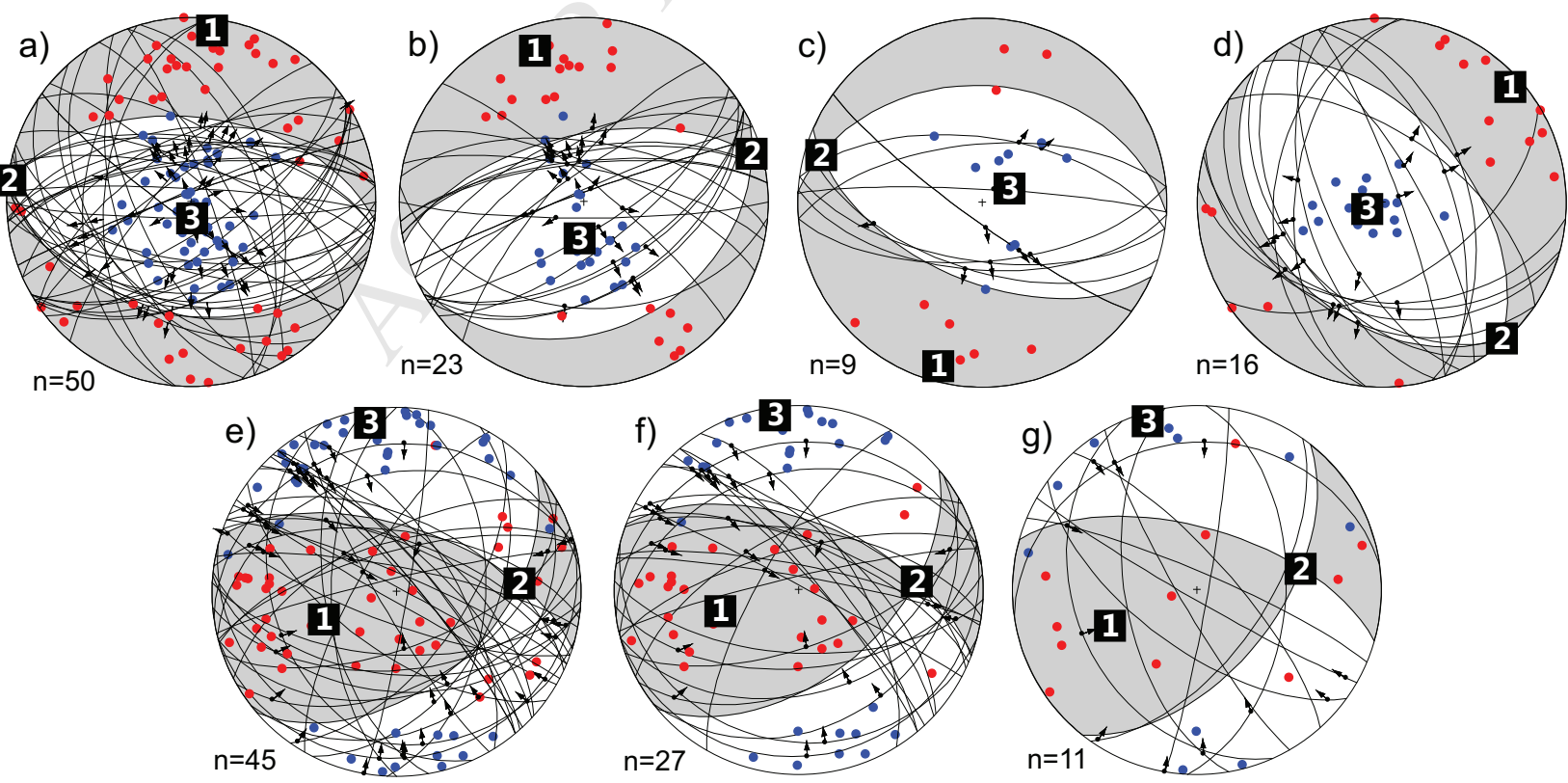


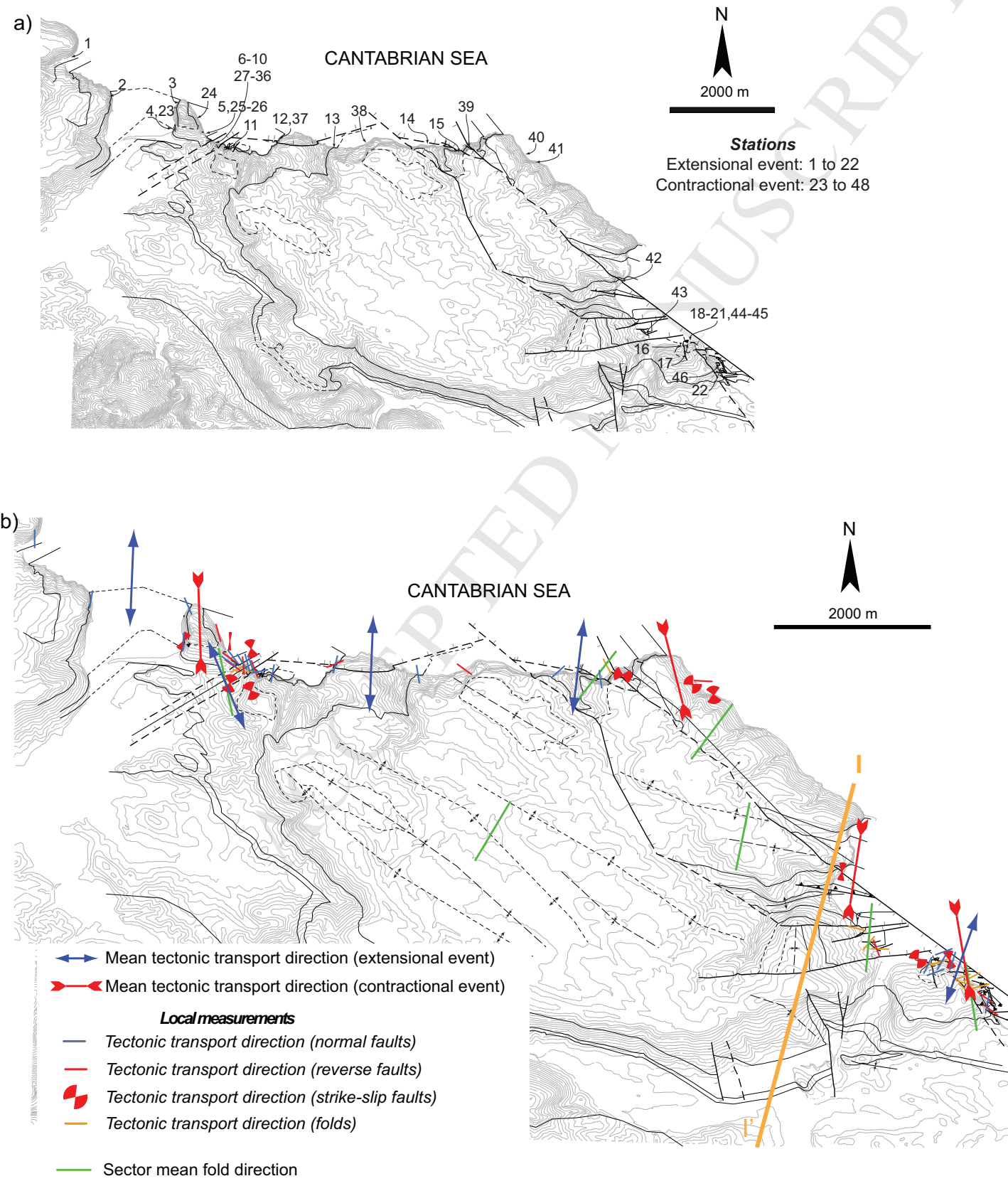


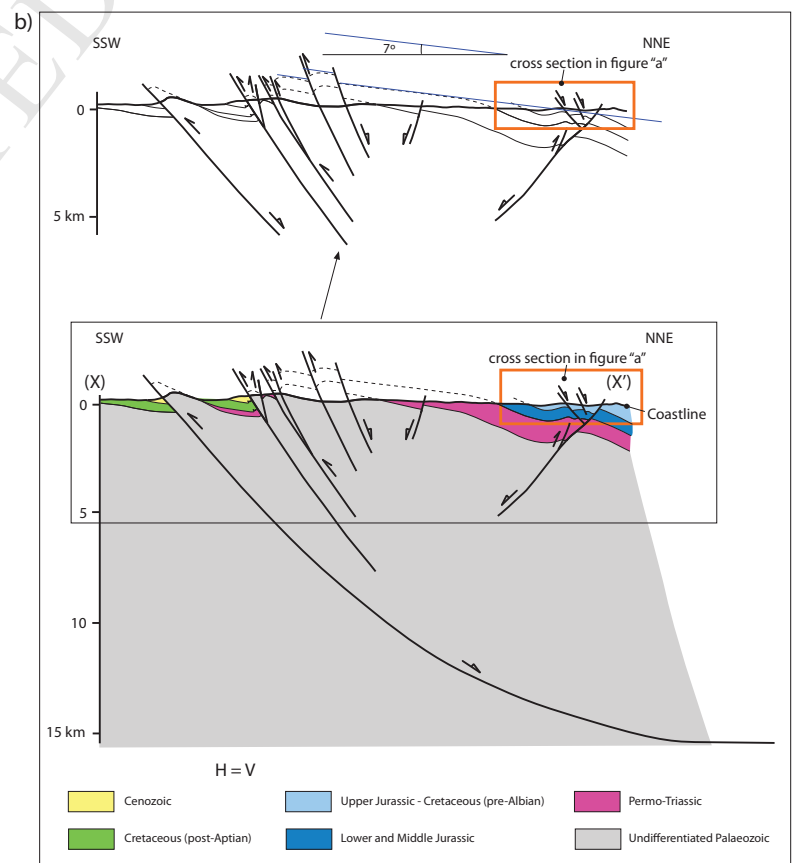
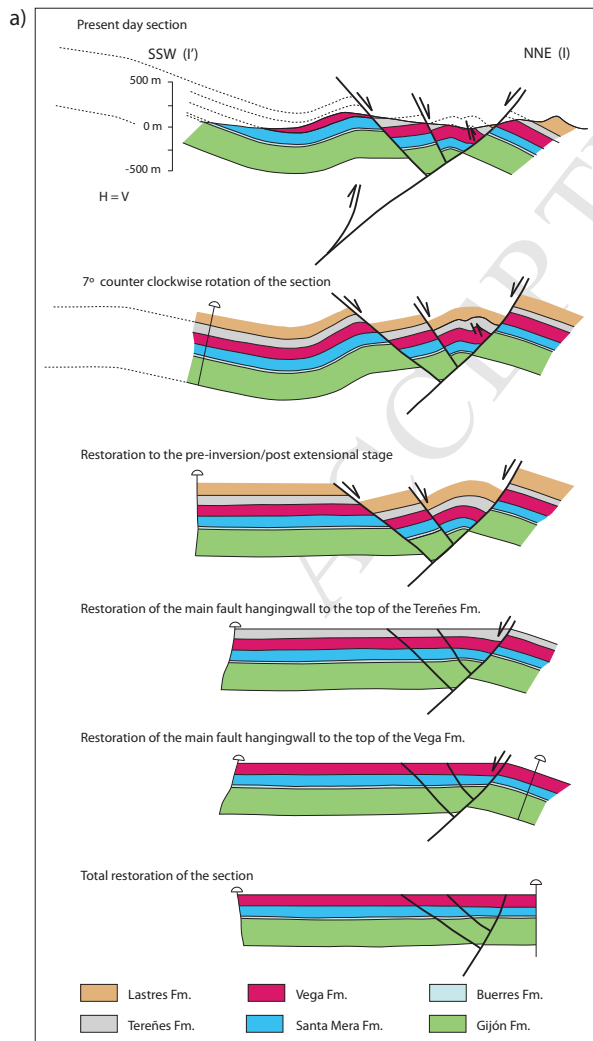


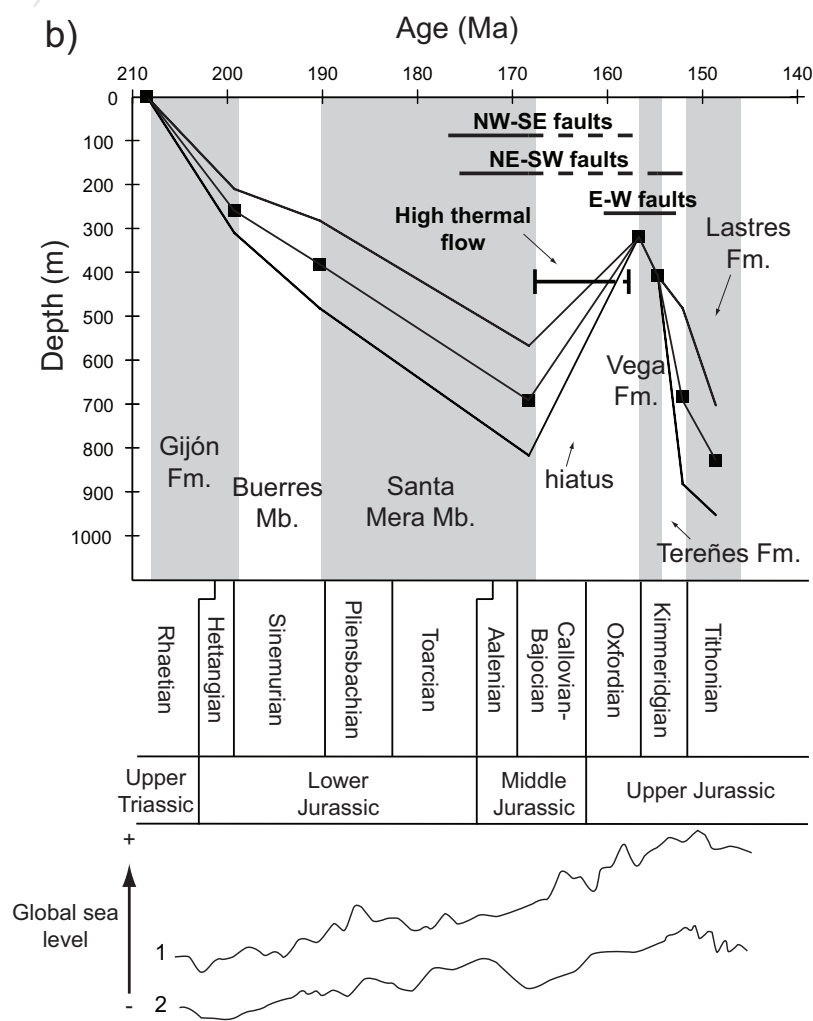
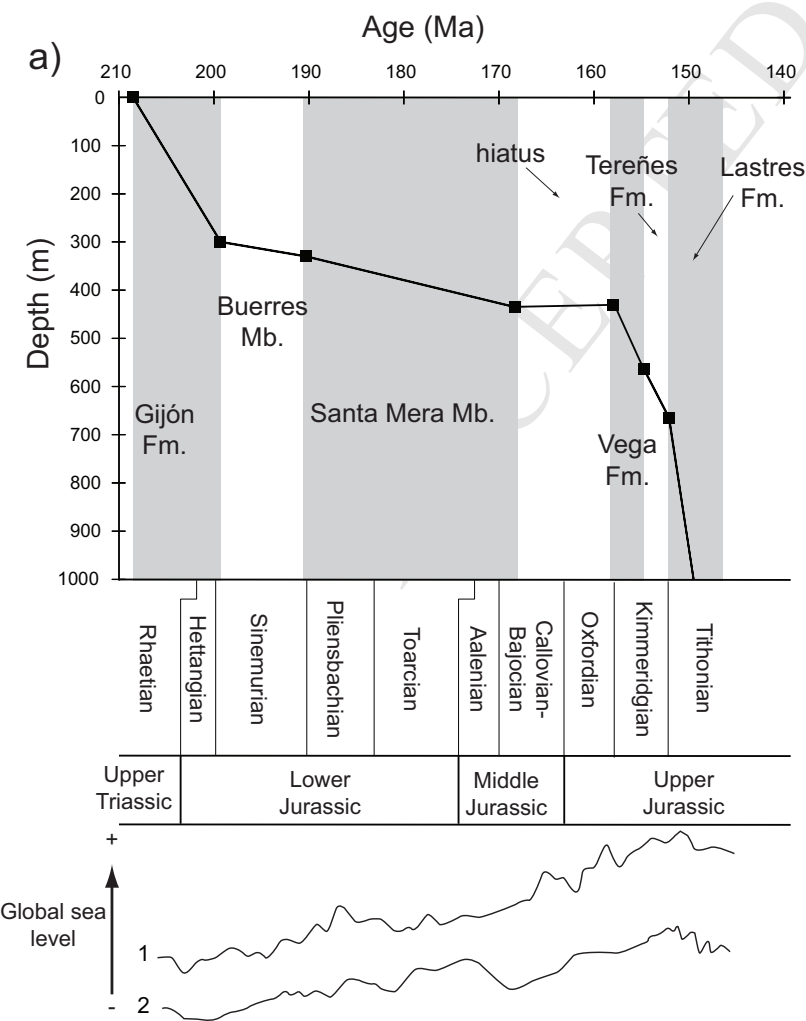
— normal fault — reverse fault



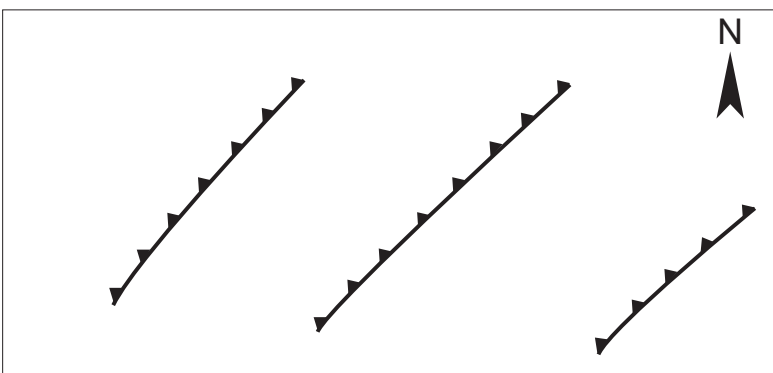




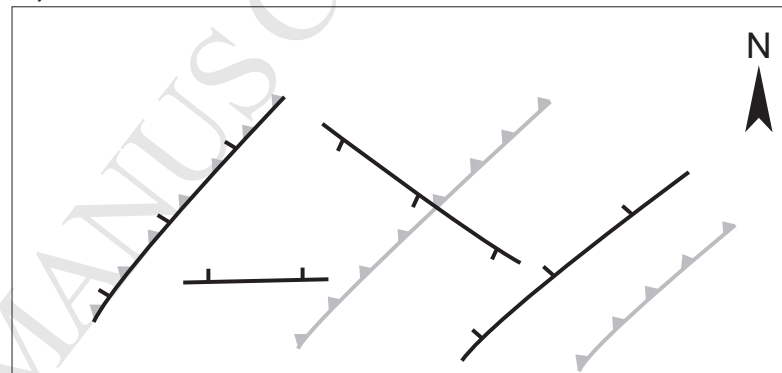




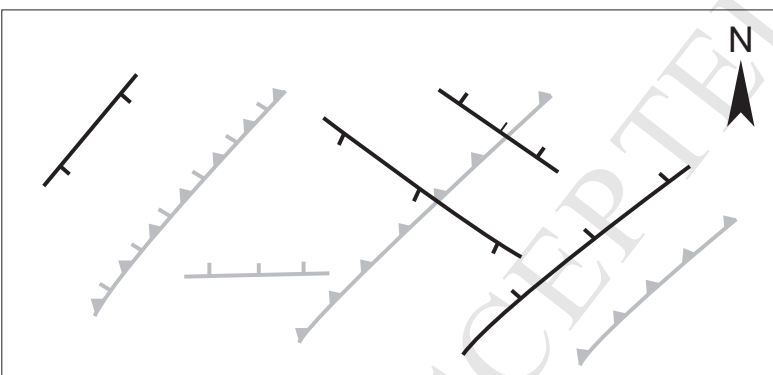
a) Carboniferous



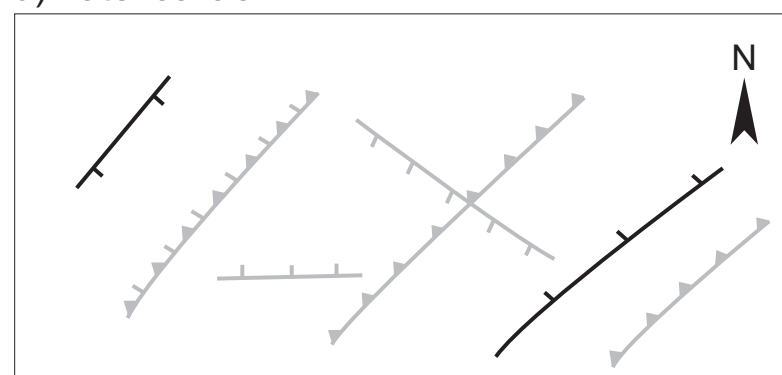
b) Permian-Triassic



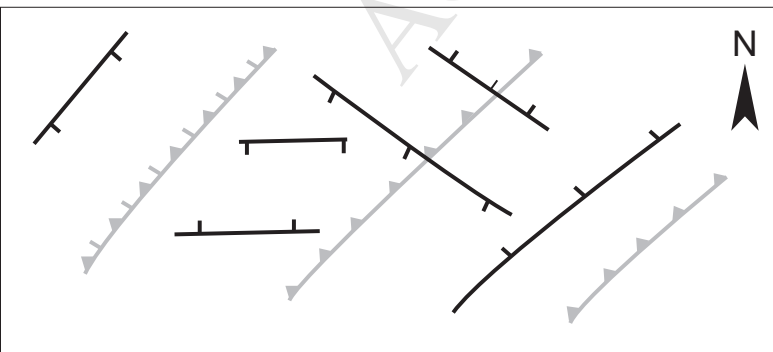
c) Middle Toarcian



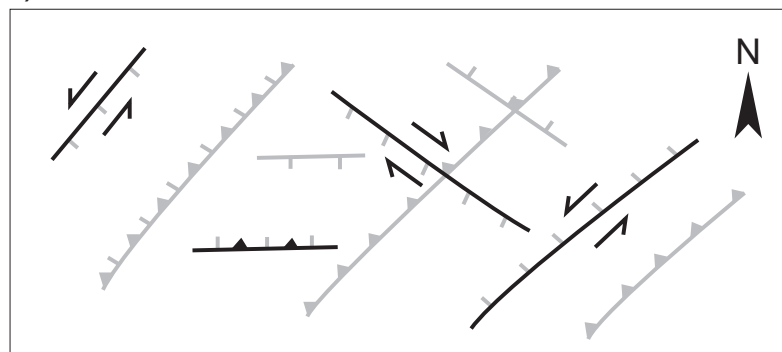
d) Late Toarcian



e) Late Jurassic (Kimmeridgian)



f) Cenozoic



Active fault
 Inactive fault

▲
▲
 Reverse fault

┐
┌
 Normal fault

↙
↘
 Strike-slip fault

HIGHLIGHTS

- Middle Jurassic normal faulting, high heat flow and basin uplift caused doming
- Increment in the normal faults displacement during Jurassic-Cretaceous
- Cenozoic contraction led to buttressing, fault reactivation and new folds and thrusts
- The Middle Jurassic event could be a precursor of the Bay of Biscay opening
- The Cenozoic event caused Cantabrian ranges uplift and Bay of Biscay partial closure